

# Three-dimensional models of elastostatic deformation in heterogeneous media, with applications to the Eastern California Shear Zone

Sylvain Barbot, Yuri Fialko and David Sandwell

*Institute of Geophysics and Planetary Physics, Scripps Institution of Oceanography, University of California San Diego, La Jolla, CA 92093-0225, USA.  
E-mail: sbarbot@ucsd.edu*

Accepted 2009 March 25. Received 2009 March 25; in original form 2008 November 19

## SUMMARY

We present a semi-analytic iterative procedure for evaluating the 3-D deformation due to faults in an arbitrarily heterogeneous elastic half-space. Spatially variable elastic properties are modelled with equivalent body forces and equivalent surface traction in a ‘homogenized’ elastic medium. The displacement field is obtained in the Fourier domain using a semi-analytic Green function. We apply this model to investigate the response of 3-D compliant zones (CZ) around major crustal faults to coseismic stressing by nearby earthquakes. We constrain the two elastic moduli, as well as the geometry of the fault zones by comparing the model predictions to Synthetic Aperture Radar interferometric (InSAR) data. Our results confirm that the CZ models for the Rodman, Calico and Pinto Mountain faults in the Eastern California Shear Zone (ECSZ) can explain the coseismic InSAR data from both the Landers and the Hector Mine earthquakes. For the Pinto Mountain fault zone, InSAR data suggest a 50 per cent reduction in effective shear modulus and no significant change in Poisson’s ratio compared to the ambient crust. The large wavelength of coseismic line-of-sight displacements around the Pinto Mountain fault requires a fairly wide ( $\sim 1.9$  km) CZ extending to a depth of at least 9 km. Best fit for the Calico CZ, north of Galway Dry Lake, is obtained for a 4 km deep structure, with a 60 per cent reduction in shear modulus, with no change in Poisson’s ratio. We find that the required effective rigidity of the Calico fault zone south of Galway Dry Lake is not as low as that of the northern segment, suggesting along-strike variations of effective elastic moduli within the same fault zone. The ECSZ InSAR data is best explained by CZ models with reduction in both shear and bulk moduli. These observations suggest pervasive and widespread damage around active crustal faults.

**Key words:** Numerical solutions; Radar interferometry; Fault zone rheology; Crustal structure; Mechanics, theory, and modelling.

## 1 INTRODUCTION

Crustal faulting is often associated with development of highly fractured and damaged rocks around the primary slip surface (Ambraseys 1970; Wilson *et al.* 2004; Chester *et al.* 2005). Such damage zones may result from distributed inelastic deformation associated with the propagation and coalescence of cracks and joints during fault growth (Segall & Pollard 1980; Vermilye & Scholz 1998; Manighetti *et al.* 2001), relaxation of stresses at geometric irregularities (Liu *et al.* 2003; Dieterich & Smith 2007) or dynamic loading at the propagating rupture front (Rice *et al.* 2005; Fialko 2007). Field observations suggest that the thickness of the cataclastic zones correlates with the cumulative fault slip (Scholz 1987). Intense damage gives rise to a reduction in the effective elastic shear modulus of the fault zone material, as predicted by theoretical models (Rybicki 1971; Kachanov 1986; Lyakhovskiy *et al.*

2001; Turcotte *et al.* 2003), and evidenced by geodetic (Chen & Freymueller 2002; Fialko *et al.* 2002; Fialko 2004; Hamiel & Fialko 2007) and seismic (Li *et al.* 1994; Ben-Zion *et al.* 2003; Thurber *et al.* 2003; Cochran *et al.* 2009) observations.

In a recent study, Cochran *et al.* (2009) showed that the geodetically inferred kilometre-wide compliant fault zones in the Mojave desert (Fialko *et al.* 2002; Fialko 2004) are also expressed in marked reductions in seismic velocities. The width of the tomographically imaged low velocity zones, as well as the magnitude of velocity reductions were found to be consistent with independent geodetic estimates. Seismic observations reveal the complex structure of the fault damage zones, with large gradients in the effective elastic moduli both laterally and as a function of depth. An accurate description of the deformation due to such fault zones requires models of fault slip in 3-D heterogeneous media. In this study, we present an efficient algorithm for simulating the deformation due

to faulting in the presence of arbitrary spatial variations in elastic properties. Several investigators have proposed ways to tackle this problem (e.g. Du *et al.* 1997; Moulinec & Suquet 1998; Pollitz 2003). The approach of Du *et al.* (1997) is limited to discrete variations in elastic properties. The method of Pollitz (2003) is more general, allowing gradual variations in elastic and viscous parameters, but the normal-mode based solution makes it less practical for small-scale problems. Moulinec & Suquet (1998) and other investigators (Lebensohn 2001; Brown *et al.* 2003; Yu *et al.* 2005) base their solution on a Fourier representation but do not include the free surface. All these semi-analytic techniques use essentially a perturbation approach and are limited to small variations in elastic properties. Our proposed method relaxes the constraint of weak inclusions and allows gradual variations in shear and bulk moduli. Our Fourier-domain semi-analytic solution is adequate for modelling intermediate-scale static deformation, such as fault slip in the presence of neighbouring compliant zones.

In the Section 2, we present the governing equations and boundary conditions relevant to a 3-D heterogeneous problem. We generalize the description of dislocations in terms of double-couple equivalent body forces by including equivalent surface traction in case of faults extending to the Earth's surface. This generalized representation allows us to model normal, reverse and strike-slip faults of arbitrary geometry. We then present some iterative methods that evaluate the displacement field based on the homogenization of elastic properties. One such method is the successive approximation (SA, Barbot *et al.* 2008); we show that it is in essence equivalent to the perturbation method (e.g. Du *et al.* 1994; Du *et al.* 1997; Pollitz 2003; Yu *et al.* 2005). The SAs and the perturbation methods are adequate for small variations in elastic properties (Moulinec & Suquet 1998; Barbot *et al.* 2008). Another approach is the successive over relaxation (SOR) method (Barbot *et al.* 2008), which allows for larger contrasts in elastic properties. Comparisons with analytic solutions and some example calculations are presented in the Appendix. We apply our numerical method to model the static deformation in the Eastern California Shear Zone (ECSZ) due to the 1992 Landers and 1999 Hector Mine earthquakes. We combine the model predictions with Synthetic Aperture Radar interferometric (InSAR) observations to refine inferences about the mechanical properties, geometry and structure of compliant zones associated with the Calico, Rodman and Pinto Mountain faults of the ECSZ.

## 2 3-D MODELS OF DEFORMATION DUE TO FAULTING IN HETEROGENEOUS MEDIA

In this section, we derive a 3-D model of elastostatic deformation in a semi-infinite solid with a free-surface boundary condition and 3-D variations in elastic properties. The formulation for 2-D antiplane deformation can be found in Barbot *et al.* (2008). We will first derive the forcing terms representing the effect of internal dislocations. Equivalent representations of dislocations include eigenstrain eq. (1), moment density eq. (6) and equivalent body forces (including the equivalent surface traction) eqs (9) and (13), respectively. We show that the governing equation is the inhomogeneous Navier's equation with non-constant coefficients and Neumann-type boundary conditions. Next we discuss some iterative solution methods based on the decomposition of the elastic moduli. Finally, we present some details on the numerical implementation and discuss results from our numerical benchmarks of the Appendix.

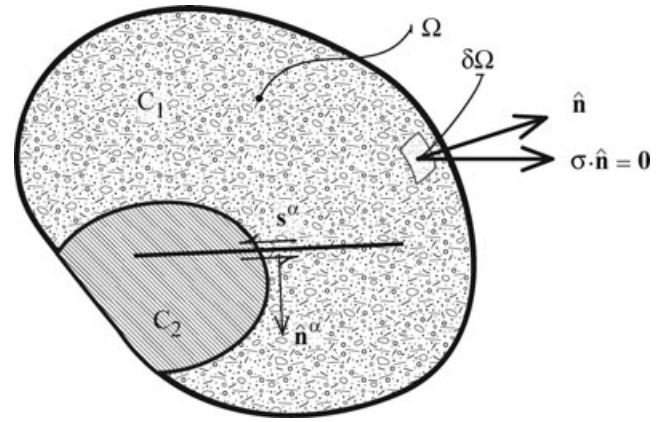


**Figure 1.** The deformation of a heterogeneous elastic body  $\Omega$  is driven by internal dislocations. A failure plane with normal  $\hat{\mathbf{n}}^\alpha$  and slip  $\mathbf{s}^\alpha$  cuts the volume with elastic tensors  $\mathbf{C}_1 \neq \mathbf{C}_2$ . The slip system  $\alpha$  is associated with eigenstrain  $\boldsymbol{\epsilon}^\alpha(\mathbf{x}) = \frac{1}{2}(\mathbf{s}^\alpha \otimes \hat{\mathbf{n}}^\alpha + \hat{\mathbf{n}}^\alpha \otimes \mathbf{s}^\alpha)$ , moment density  $\mathbf{m}^\alpha(\mathbf{x}) = \mathbf{C} : \mathbf{s}^\alpha \otimes \hat{\mathbf{n}}^\alpha$  and equivalent body force  $\mathbf{f}^\alpha(\mathbf{x}) = -\nabla \cdot \mathbf{m}^\alpha$ . The surface boundary  $\partial\Omega$ , with normal vector  $\hat{\mathbf{n}}$ , is traction free ( $\boldsymbol{\sigma} \cdot \hat{\mathbf{n}} = 0$ ).

### 2.1 Governing equation and boundary conditions

Consider a heterogeneous elastic body  $\Omega$  comprised of two interfaced volumes with dissimilar elastic properties cut by a shear dislocation  $\alpha$  (see Fig. 1). The surface of the elastic body  $\partial\Omega$  is assumed to be traction free. A dislocation characterized by slip  $\mathbf{s}^\alpha$  on a surface with normal vector  $\hat{\mathbf{n}}^\alpha$  is associated with the eigenstrain tensor (Backus & Mulcahy 1976b; Nemat-Nasser 2004; Barbot *et al.* 2008; Barbot *et al.* 2009)

$$\boldsymbol{\epsilon}^\alpha(\mathbf{x}) = \frac{1}{2}(\mathbf{s}^\alpha \otimes \hat{\mathbf{n}}^\alpha + \hat{\mathbf{n}}^\alpha \otimes \mathbf{s}^\alpha), \quad (1)$$

where operator  $\otimes$  is the dyadic product (for example, if  $\mathbf{a}$  and  $\mathbf{b}$  are two vectors, then in index notation the product  $\mathbf{a} \otimes \mathbf{b}$  is the second-order tensor  $a_i b_j$ ). Both  $\hat{\mathbf{n}}^\alpha$  and  $\mathbf{s}^\alpha$  may in general vary along the dislocation surface. The eigenstrain depends on the geometry of a dislocation but is independent of elastic properties of the ambient solid. The static deformation undergone by body  $\Omega$  compared to a reference state is characterized by the total strain  $\boldsymbol{\epsilon}$ , the sum of elastic and inelastic strains

$$\boldsymbol{\epsilon} = \boldsymbol{\epsilon}^e + \boldsymbol{\epsilon}^i, \quad (2)$$

where  $\boldsymbol{\epsilon}^i$  is the total inelastic eigenstrain due to internal dislocations

$$\boldsymbol{\epsilon}^i(\mathbf{x}) = \sum_{\alpha=1}^n \boldsymbol{\epsilon}^\alpha(\mathbf{x}), \quad (3)$$

where  $n$  is the total number of dislocations. The eigenstrain (3) is a tensor-valued forcing term and should not be confused with the elastic strain in the near field of the dislocation. Note that the eigenstrain tensor is identically zero away from a dislocation. In general, any degree of localization of eigenstrain can be represented using generalized functions such as boxcar or Dirac-delta functions. For discussions and examples on the use of generalized functions for body-force representation, see Backus & Mulcahy (1976b), Barbot *et al.* (2008, 2009). In a heterogeneous body  $\Omega$  with the tensor of elastic moduli  $\mathbf{C} = \mathbf{C}(\mathbf{x})$ , the Cauchy stress

$$\boldsymbol{\sigma} = \mathbf{C} : \boldsymbol{\epsilon}^e, \quad (4)$$

where operation  $:$  is the double scalar product (for instance, if  $\mathbf{A}$  and  $\mathbf{B}$  are two second-order tensors, then in index notation the product

$\mathbf{A} : \mathbf{B}$  is the scalar  $A_{ij}B_{ij}$ ), can be written using eq. (2) as follows:

$$\boldsymbol{\sigma} = \mathbf{C} : \boldsymbol{\epsilon} - \mathbf{C} : \boldsymbol{\epsilon}^i, \quad (5)$$

where the second term can be recognized as the moment density (Aki & Richards 1980; Shearer 1999)

$$\mathbf{m}(\mathbf{x}) = \sum_{\alpha=1}^n \mathbf{C}(\mathbf{x}) : \boldsymbol{\epsilon}^\alpha. \quad (6)$$

As elastic properties are spatially variable, the moment density is not necessarily uniform along a dislocation surface. Using eq. (5), the conservation of momentum for static equilibrium in  $\Omega$  can be written (Malvern 1969; Nemat-Nasser & Hori 1999)

$$\nabla \cdot (\mathbf{C} : \boldsymbol{\epsilon}) - \nabla \cdot (\mathbf{C} : \boldsymbol{\epsilon}^i) = 0. \quad (7)$$

The second term in eq. (7) depends upon the distribution and orientation of internal dislocations in  $\Omega$ . The effect of all internal dislocations may be represented using equivalent body forces (Eshelby 1957; Burridge & Knopoff 1964; Nemat-Nasser 2004)

$$\mathbf{f}(\mathbf{x}) = -\nabla \cdot (\mathbf{C} : \boldsymbol{\epsilon}^i) = \sum_{\alpha=1}^n \mathbf{f}^\alpha(\mathbf{x}), \quad (8)$$

where

$$\mathbf{f}^\alpha(\mathbf{x}) = -\nabla \cdot (\mathbf{C} : \mathbf{s}^\alpha \otimes \hat{\mathbf{n}}^\alpha) \quad (9)$$

is the equivalent body-force density due to an individual dislocation  $\alpha$ , and  $\mathbf{s}^\alpha$  and  $\hat{\mathbf{n}}^\alpha$  refer to the Burger's vector and the normal direction of dislocation  $\alpha$ , respectively. As dislocations may cut across heterogeneous regions, the equivalent body force (9) may not be readily reduced to a double couple. The conservation of momentum can now be written as

$$\nabla \cdot (\mathbf{C} : \boldsymbol{\epsilon}) + \mathbf{f} = 0, \quad (10)$$

where

$$\boldsymbol{\epsilon} = \frac{1}{2} [\nabla \otimes \mathbf{u} + (\nabla \otimes \mathbf{u})^T] \quad (11)$$

is the total strain and  $\mathbf{u}(\mathbf{x})$  is the associated displacement. Governing eq. (10) simplifies to the Navier's equation for a homogeneous isotropic elastic medium. The equivalent body force density  $\mathbf{f}(\mathbf{x})$  depends upon the elastic structure  $\mathbf{C}(\mathbf{x})$ . The force distribution represents the effect of all internal dislocations and for now is supposed to be known.

We seek the displacement field  $\mathbf{u}(\mathbf{x})$  within  $\Omega$  that satisfies governing eq. (10) subject to the free surface boundary condition. The surface traction can be expressed in terms of the total strain,

$$\begin{aligned} \boldsymbol{\sigma} \cdot \hat{\mathbf{n}} &= \hat{\mathbf{n}} \cdot (\mathbf{C} : \boldsymbol{\epsilon}^e) \\ &= \hat{\mathbf{n}} \cdot (\mathbf{C} : \boldsymbol{\epsilon}) - \hat{\mathbf{n}} \cdot (\mathbf{C} : \boldsymbol{\epsilon}^i) \end{aligned} \quad (12)$$

so that dislocations cutting through the boundary  $\partial\Omega$  contribute to the equivalent surface traction as follows:

$$\begin{aligned} \mathbf{t} &= \hat{\mathbf{n}} \cdot (\mathbf{C} : \boldsymbol{\epsilon}^i) \\ &= \sum_{\alpha=1}^n \hat{\mathbf{n}} \cdot (\mathbf{C} : \mathbf{s}^\alpha \otimes \mathbf{n}^\alpha), \end{aligned} \quad (13)$$

where  $\mathbf{n}^\alpha$  and  $\mathbf{s}^\alpha$  are evaluated at the surface. The equivalent surface traction due to a dislocation  $\alpha$  is therefore

$$\mathbf{t}^\alpha = \hat{\mathbf{n}} \cdot (\mathbf{C} : \mathbf{s}^\alpha \otimes \mathbf{n}^\alpha). \quad (14)$$

The presence of non-vanishing equivalent surface traction depends upon the relative orientation of the normal direction at the surface

$\partial\Omega$  and the moment density  $\mathbf{m}^\alpha = \mathbf{C} : (\mathbf{s}^\alpha \otimes \hat{\mathbf{n}}^\alpha)$  of dislocations that cut the surface (Backus & Mulcahy 1976a). A vertical strike-slip fault at the surface of a half-space, for example, is not associated with equivalent surface traction. Fig. 2 shows the equivalent body-force distribution and the equivalent normal traction due to a given point dislocation intersecting the surface of a half-space in case of isotropic elasticity. The moment density of dislocation  $\alpha$  with arbitrary direction is decomposed into six linearly independent directions in a symmetric tensor space. Whereas equivalent body forces for a point-source dislocation simplify to a double couple, the equivalent surface traction  $\mathbf{t}^\alpha$  simplifies to a simple traction vector: purely tangential traction for off-diagonal moment density components and purely normal traction for diagonal components. Equivalent body forces and equivalent surface traction are dual through the application of the divergence theorem. Using eq. (12), the free surface boundary condition in the presence of dislocations at the surface of  $\Omega$  can be written as

$$\hat{\mathbf{n}} \cdot (\mathbf{C} : \boldsymbol{\epsilon}) = \mathbf{t} = \sum_{\alpha=1}^n \mathbf{t}^\alpha \quad \text{on } \partial\Omega. \quad (15)$$

Internal dislocations and associated boundary conditions can therefore be reduced to some equivalent body-force density  $\mathbf{f}(\mathbf{x})$  in  $\Omega$  and some equivalent normal traction  $\mathbf{t}$  on  $\partial\Omega$ . In the case of homogeneous and isotropic elasticity, the problem simplifies to Navier's equation with forcing terms and inhomogeneous boundary conditions.

## 2.2 Decomposition of elastic moduli

Our approach to solving the governing eq. (10) subject to boundary condition (15) consists in using the elastic Green function for a homogeneous medium and in identifying a set of equivalent body force and equivalent surface traction that represents the effect of spatial variations in elastic properties.

Consider the following decomposition of the elastic moduli tensor  $\mathbf{C}(\mathbf{x})$  into a constant, homogeneous part  $\mathbf{C}_0$  and a spatially variable part  $\mathbf{C}'(\mathbf{x})$ , such that

$$\mathbf{C}(\mathbf{x}) = \mathbf{C}_0 - \mathbf{C}'(\mathbf{x}). \quad (16)$$

We define

$$\boldsymbol{\sigma}' = \mathbf{C}' : \boldsymbol{\epsilon}, \quad (17)$$

the moment density corresponding to spatial variations in elastic properties. Using eqs (10) and (16), we now can write the governing equation as follows:

$$\nabla \cdot (\mathbf{C}_0 : \boldsymbol{\epsilon}) + \mathbf{f} - \nabla \cdot \boldsymbol{\sigma}' = 0. \quad (18)$$

The variations in elastic properties introduce the moment density  $\mathbf{m}' = \mathbf{C}' : \nabla \otimes \mathbf{u}$  and the equivalent body-force representation of the effects of the inhomogeneous elastic properties in the 'homogenized' medium is

$$\mathbf{f}'(\mathbf{x}) = -\nabla \cdot \boldsymbol{\sigma}'. \quad (19)$$

Note that the body force representation for dislocations is unaffected by the elastic moduli decomposition. The moment density introduced by internal dislocations is a function of the actual elastic properties  $\mathbf{C}(\mathbf{x})$  of the body. Making use of eq. (16), the surface traction becomes

$$\begin{aligned} \boldsymbol{\sigma} \cdot \hat{\mathbf{n}} &= \hat{\mathbf{n}} \cdot (\mathbf{C}_0 : \boldsymbol{\epsilon}) \\ &\quad - \hat{\mathbf{n}} \cdot (\mathbf{C}' : \boldsymbol{\epsilon}) - \hat{\mathbf{n}} \cdot (\mathbf{C} : \boldsymbol{\epsilon}^i) = 0. \end{aligned} \quad (20)$$

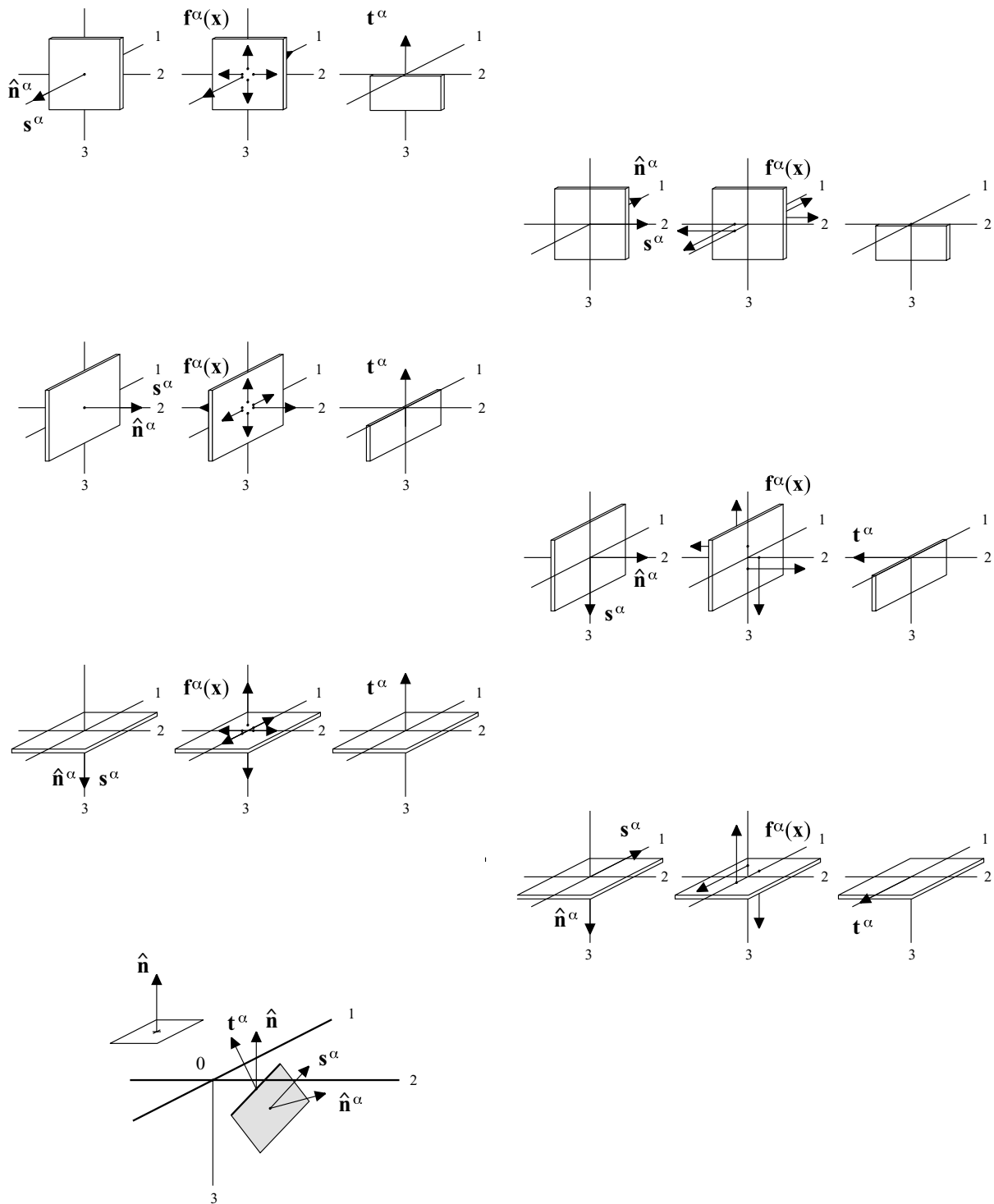


**Figure 2.** An arbitrary slip system  $\alpha$  for a point source dislocation (bottom sketch) can be decomposed into six linearly independent components. Eigenstrain  $\epsilon^\alpha$  is associated with an equivalent body force distribution  $\mathbf{f}^\alpha(\mathbf{x})$  and equivalent surface traction  $\mathbf{t}^\alpha$ . Equivalent surface traction occurs when fractures reach to the surface of the semi-infinite solid.

Consequently, the free surface boundary condition in the homogenized body can be expressed as follows:

$$\hat{\mathbf{n}} \cdot (\mathbf{C}_0 : \boldsymbol{\epsilon}) = \mathbf{t} + \mathbf{t}' \quad \text{on } \partial\Omega, \quad (21)$$

where

$$\mathbf{t}' = \boldsymbol{\sigma}' \cdot \hat{\mathbf{n}} \quad (22)$$

is the surface traction due to deviations from the homogenized elastic properties at the surface  $\partial\Omega$ . In case of a layered medium, if  $\mathbf{C}_0$  is chosen to correspond to the value of  $\mathbf{C}(\mathbf{x})$  in the top layer, the additional equivalent surface traction simply vanishes as  $\mathbf{C}'(\mathbf{x}) = 0$  on  $\partial\Omega$ . Similar to the equivalent body forces, the equivalent surface traction  $\mathbf{t}$  due to internal dislocations is unaffected by the decomposition of the elastic moduli tensor.

Decomposition (16) allows us to transform an equation with non-constant coefficients into a homogeneous equation with modified boundary conditions and additional internal forcing terms. For known equivalent body forces and surface traction representing the elastic heterogeneity, the solution for a displacement field is (Aki & Richards 1980)

$$\mathbf{u}(\mathbf{x}) = \int_{\Omega} \mathbf{G}(\mathbf{x}, \mathbf{x}_0) \cdot [\mathbf{f}(\mathbf{x}_0) + \mathbf{f}'(\mathbf{x}_0)] d\mathbf{x}_0 + \int_{\partial\Omega} \mathbf{G}(\mathbf{x}, \mathbf{x}_0) \cdot [\mathbf{t}(\mathbf{x}_0) + \mathbf{t}'(\mathbf{x}_0)] d\mathbf{x}_0, \quad (23)$$

where  $\mathbf{G}(\mathbf{x}, \mathbf{x}_0)$  is the Green function tensor (see Love 1927; Mindlin 1936, for the case of a semi-infinite solid) for an elastic body with a homogeneous elastic moduli tensor  $\mathbf{C}_0$ . However, one cannot readily evaluate eq. (23), as the distribution of body forces mimicking the presence of heterogeneities needs to be determined as part of the solution.

### 2.3 The successive approximation method

One way to solve the heterogeneous problem (eq. 23) is to use the method of SAs (Bender & Orszag 1978; Kato 1980; Delves & Mohamed 1985). Extending the approach proposed by Barbot *et al.* (2008) to the case of 3-D deformation, we adopt the following iterative procedure

$$\mathbf{u}_n(\mathbf{x}) = \int_{\Omega} \mathbf{G} \cdot [\mathbf{f} - \nabla \cdot (\mathbf{C}' : \nabla \mathbf{u}_{n-1})] dV + \int_{\partial\Omega} \mathbf{G} \cdot [\mathbf{t} + (\mathbf{C}' : \nabla \mathbf{u}_{n-1}) \cdot \hat{\mathbf{n}}] dA, \quad (24)$$

where index  $n$  denotes a level of approximation. Noticing integrals in eq. (24) are linear with respect to  $\mathbf{u}$ , we define an operator

$$\mathcal{L}[\mathbf{v}] = - \int_{\Omega} \mathbf{G} \cdot [\nabla \cdot (\mathbf{C}' : \nabla \mathbf{v})] dV + \int_{\partial\Omega} \mathbf{G} \cdot [(\mathbf{C}' : \nabla \mathbf{v}) \cdot \hat{\mathbf{n}}] dA, \quad (25)$$

where  $\mathbf{v}$  is a vector field in  $\Omega$ . We then define the first non-zero term in series (24)

$$\mathbf{u}_0(\mathbf{x}) = \int_{\Omega} \mathbf{G}(\mathbf{x}, \mathbf{x}_0) \cdot \mathbf{f}(\mathbf{x}_0) d\mathbf{x}_0 + \int_{\partial\Omega} \mathbf{G}(\mathbf{x}, \mathbf{x}_0) \cdot \mathbf{t}(\mathbf{x}_0) dA. \quad (26)$$

Using eqs (25) and (26), the proposed iterative procedure (24) can now be written as

$$\mathbf{u}_n(\mathbf{x}) = \mathbf{u}_0(\mathbf{x}) + \mathcal{L}[\mathbf{u}_{n-1}], \quad (27)$$

where  $\mathbf{u}_0(\mathbf{x})$  is the first approximate solution, and the true solution to the heterogeneous problem is (assuming non-biased convergence)

$$\mathbf{u}(\mathbf{x}) = \lim_{n \rightarrow \infty} \mathbf{u}_n(\mathbf{x}). \quad (28)$$

We refer to formulation (24)–(27) as the SA method to evaluate the solution of the heterogeneous elastic problem governed by eq. (10) with boundary condition (15). The SA method is used in various geophysical contexts including flexure of the oceanic lithosphere (Sandwell 1984), mantle convection (Gable *et al.* 1991), deformation of heterogeneous mineral composites (Moulinec & Suquet 1998; Lebensohn 2001; Brown *et al.* 2003) and volcano geodesy (Fialko *et al.* 2001a). Iterative methods such as the SA allow one to handle complex media for which an exact Green function is not readily available.

### 2.4 The perturbation method

The SA series (27) can be reorganized in a form of an infinite sum (Kato 1980)

$$\mathbf{u}_n = \mathbf{u}^{(0)} + \sum_{k=1}^n \mathbf{u}^{(k)}, \quad n \in \mathbb{N}^* \quad (29)$$

with the recursive relation

$$\mathbf{u}^{(k)} = \mathcal{L}[\mathbf{u}^{(k-1)}] \quad (30)$$

and initial value

$$\mathbf{u}^{(0)} \equiv \mathbf{u}_0(\mathbf{x}). \quad (31)$$

The proof can be obtained by recurrence: consider the first iteration of the SA solution

$$\begin{aligned} \mathbf{u}_1 &= \mathbf{u}_0 + \mathcal{L}[\mathbf{u}_0] = \mathbf{u}^{(0)} + \mathcal{L}[\mathbf{u}^{(0)}] \\ &= \mathbf{u}^{(0)} + \sum_{k=1}^1 \mathcal{L}[\mathbf{u}^{(k)}]. \end{aligned} \quad (32)$$

Assuming that eqs (29) and (30) hold true for  $n > 1$ , we consider iteration  $n + 1$

$$\begin{aligned} \mathbf{u}_{n+1} &= \mathbf{u}_0 + \mathcal{L}[\mathbf{u}_n] \\ &= \mathbf{u}^{(0)} + \mathcal{L} \left[ \mathbf{u}^{(0)} + \sum_{k=1}^n \mathbf{u}^{(k)} \right] \\ &= \mathbf{u}^{(0)} + \mathcal{L}[\mathbf{u}^{(0)}] + \sum_{k=1}^n \mathcal{L}[\mathbf{u}^{(k)}] \\ &= \mathbf{u}^{(0)} + \mathbf{u}^{(1)} + \sum_{k=1}^n \mathbf{u}^{(k+1)} \\ &= \mathbf{u}^{(0)} + \sum_{k=1}^{n+1} \mathbf{u}^{(k)}, \end{aligned} \quad (33)$$

where we took advantage of the fact that  $\mathcal{L}$  is a linear operator and thus can be moved inside the sum. As eqs (29) and (30) hold at iteration  $n$ , they must also hold at iteration  $n + 1$ . Therefore, we have shown by recurrence that the SA series (27) can be written as the finite sum (29). The ultimate solution associated with the recurrence relation (30) is therefore

$$\mathbf{u}(\mathbf{x}) = \mathbf{u}^{(0)}(\mathbf{x}) + \sum_{n=1}^{\infty} \mathbf{u}^{(n)}(\mathbf{x}). \quad (34)$$

Formulation (34) is referred to as the perturbation method to solve eq. (23). The perturbation method was used by Du *et al.* (1994), Du *et al.* (1997) to model deformation due to faulting in heterogeneous media with some limiting assumptions about the spatial variations of elastic moduli. Our approach allows one to model gradual changes in elastic moduli as well as to evaluate numerically virtually any number of higher-order approximations of the true solution.

### 2.5 The successive over relaxation method

The SOR technique (Press *et al.* 1992; Barbot *et al.* 2008) is a minor modification of the SA method. Defining a linear operator

$$\begin{aligned} T[\mathbf{v}] &= \int_{\Omega} \mathbf{G} \cdot [\mathbf{f} - \nabla \cdot (\mathbf{C}' : \nabla \mathbf{v})] dV \\ &+ \int_{\partial\Omega} \mathbf{G} \cdot [\mathbf{t} + (\mathbf{C}' : \nabla \mathbf{v}) \cdot \hat{\mathbf{n}}] dA, \end{aligned} \quad (35)$$

where  $\mathbf{v}$  is a vector field in  $\Omega$ , the SA method can be written as

$$\mathbf{u}_n = T[\mathbf{u}_{n-1}]. \quad (36)$$

A natural way of regularizing the numerical evaluation of eq. (36) is to use the SOR method (Golub & Van Loan 1996). The iterative procedure becomes

$$\mathbf{u}_n = (1 - \phi) \mathbf{u}_{n-1} + \phi T[\mathbf{u}_{n-1}], \quad (37)$$

where  $0 < \phi < 2$  is the SOR parameter. Obviously, the SOR method simplifies to the SA or the perturbation method for  $\phi = 1$ . Solutions for cracked media with large variations in elastic properties can be obtained using  $\phi \simeq 0.5$  when the homogenized elastic tensor satisfies certain conditions (e.g. see eq. 43).

In practice, we use only a limited number of terms in the SOR series (37) or the perturbation method series (34). An estimate of the body force representing the presence of faults and variable elastic moduli is

$$\tilde{\mathbf{f}}_n = \mathbf{f} - \nabla \cdot (\mathbf{C}' : \nabla \mathbf{u}_n), \quad (38)$$

and a common convergence criterion for the SA and SOR methods is

$$\frac{\langle \|\tilde{\mathbf{f}}_n\|^2 \rangle - \langle \|\tilde{\mathbf{f}}_{n-1}\|^2 \rangle}{\langle \|\mathbf{f}\|^2 \rangle} < \epsilon, \quad (39)$$

where  $\epsilon$  is the tolerance (hereafter, we use  $\epsilon = 10^{-6}$ ), and the angular bracket operator  $\langle \cdot \rangle$  denotes integration over the domain  $\Omega$ .

## 2.6 Homogenization of elastic moduli

The perturbation and the SA methods are adequate only in case of small variations in elastic properties (Moulinec & Suquet 1998; Barbot *et al.* 2008). For instance, in case of antiplane deformation, a necessary convergence criterion is satisfied when rigidity contrasts are less than a factor of two of the homogenized value (Barbot *et al.* 2008). In the case of an isotropic heterogeneous body under condition of antiplane strain, the fastest convergence of the SA method is obtained for a homogenized rigidity that minimizes the maximum effective rigidity contrast in the body (Barbot *et al.* 2008). To generalize this result to 3-D deformation, we note that the isotropic elastic tensor can be decomposed into the pure volumetric and pure shear directions in tensor space,  $\mathbf{E}_1$  and  $\mathbf{E}_2$ , respectively (Hill 1965; Nemat-Nasser & Hori 1999)

$$\mathbf{E}_1 = \frac{1}{3} \mathbf{1}^{(2)} \otimes \mathbf{1}^{(2)}, \quad \mathbf{E}_2 = \mathbf{1}^{(4s)} - \frac{1}{3} \mathbf{1}^{(2)} \otimes \mathbf{1}^{(2)}, \quad (40)$$

where  $\mathbf{1}^{(4s)}$  is the symmetric and unitary fourth-order tensor and  $\mathbf{1}^{(2)}$  is the second-order unitary tensor. Tensors  $\mathbf{E}_1$  and  $\mathbf{E}_2$  satisfy the orthonormality relations

$$\begin{aligned} \mathbf{E}_1 &= \mathbf{E}_1 : \mathbf{E}_1 \\ \mathbf{E}_2 &= \mathbf{E}_2 : \mathbf{E}_2 \\ \mathbf{E}_1 : \mathbf{E}_2 &= \mathbf{E}_2 : \mathbf{E}_1 = 0 \end{aligned} \quad (41)$$

and form a base for any isotropic fourth-order tensor. The isotropic elastic moduli tensor can therefore be written as

$$\mathbf{C}(\mathbf{x}) = 3\kappa(\mathbf{x}) \mathbf{E}_1 + 2G(\mathbf{x}) \mathbf{E}_2, \quad (42)$$

where  $\kappa = \lambda + 2G/3$  and  $G$  are the bulk and shear moduli that can vary spatially. As strain directions  $\mathbf{E}_1$  and  $\mathbf{E}_2$  are orthogonal, the constraints on the elastic moduli tensor reduce to independent constraints on scalars  $\kappa$  and  $G$ . Consequently, we choose the following

values for the homogenized elastic parameters

$$\begin{aligned} G_0 &= \frac{1}{2} \left[ \max_{\Omega} G(\mathbf{x}) + \min_{\Omega} G(\mathbf{x}) \right] \\ \kappa_0 &= \frac{1}{2} \left[ \max_{\Omega} \kappa(\mathbf{x}) + \min_{\Omega} \kappa(\mathbf{x}) \right]. \end{aligned} \quad (43)$$

Given  $\lambda_0 = \kappa_0 - 2G_0/3$ , the homogenized isotropic tensor is therefore

$$\mathbf{C}_0 = \lambda_0 \mathbf{1}^{(2)} \otimes \mathbf{1}^{(2)} + 2G_0 \mathbf{1}^{(4s)}. \quad (44)$$

In the Appendix, we demonstrate that the numerical constraint of small variations in elastic properties within volume  $\Omega$  can indeed be relaxed by application of the SOR technique.

## 2.7 Implementation

We adopt a numerical approach presented by Barbot *et al.* (2008) for 2-D antiplane strain and generalize it to the case of 3-D deformation. Sources of deformation include tensile cracks and strike-slip and dip-slip faults of arbitrary orientation and position in the half-space. Note that equivalent surface traction and the equivalent body forces appear in the representation of both the forcing terms due to internal dislocations and the effect of inclusions. Models of deformation in a homogeneous half-space or in a 3-D heterogeneous half-space can therefore be evaluated with the same elastic Green function, one which satisfies a prescribed traction boundary condition at the surface.

We perform the convolution between the equivalent body forces and the Green function for the homogeneous elastic half-space numerically in the Fourier domain. The expansion of the displacement field in a Fourier series introduces a periodicity in the solution that limits the solution accuracy near the edges of the computational grid. We mitigate this bias by using large computational domains, such that deformation sources are sufficiently far from the boundaries (except the free surface). We take advantage of the convolution theorem and the fast Fourier transforms to reduce the computational burden (compared, e.g. to convolutions in the space domain). We use the Boussinesq's (Steketee 1958a,b) and Cerruti's (Love 1927; Mindlin 1936) solutions for normal and tangential surface loading, respectively, to satisfy the free surface boundary condition.

We compute the gradient of the displacement field and the divergence of the moment density using finite impulse differentiator filters (FIR) (McClellan *et al.* 1973; Farid & Simoncelli 2004) in the bulk of the half-space, and simple finite difference schemes near the surface, in the vertical direction. The impulse response of finite difference filters has a narrow bandwidth so using FIR filters allows us to compute more precise and more localized derivatives. Numerical evaluation of derivatives is critical to preserve the accuracy throughout multiple iterations in both the perturbation and the SOR methods. We taper the dislocations using the  $\Omega_\beta$  function (see eq. 17 in Barbot *et al.* 2008) to obtain band-limited sources and limit a potential Gibbs phenomenon (Bracewell 2003) in the resulting displacement field near the faults. The tapering also suppresses the stress singularity at a fault tip.

The numerical technique was extensively validated against analytic solutions for antiplane-strain problems with lateral and vertical layering (Barbot *et al.* 2008). The accuracy of dislocation models that use the Fourier-domain Green function in a 3-D homogeneous half-space is discussed in (Barbot *et al.* 2009, appendix B3). We performed some additional benchmarks for 3-D deformation in a 3-D heterogeneous half-space in the Appendix. These tests include cases of vertical and lateral variations in elastic properties,

models of faults cutting through different elastic materials, large elasticity contrasts using the SOR method and forcing terms due to strike-slip and dip-slip faults. In general, the accuracy of the iterative solution away from the (periodic) boundary is about 5–10 per cent of the expected elastic structure contribution, the largest error arising from the strongest elastic contrast: If the expected signal due to the rigidity variation is 10 per cent of the total displacement, then our numerical solution is associated with a 0.5–1 per cent bias. The accuracy of our method as shown by comparisons with other analytic, semi-analytic or numerical solutions and our ability to include complex geometric structures makes this approach adequate to model deformation due to faulting in a heterogeneous crust.

### 3 APPLICATION TO COMPLIANT FAULT ZONES IN THE MOJAVE DESERT

The ECSZ is a region of active deformation that strikes northwest-southeast across the central Mojave desert (Savage *et al.* 1980; Dokka & Travis 1990a,b; Sauber *et al.* 1994). The ECSZ extends from the San Gorgonio bend of the San Andreas fault in the south to Owens Valley and the northern Basin and Range province. A system of young strike-slip faults comprising the ECSZ accommodates 8–14 mm yr<sup>-1</sup> of motion between the North American and Pacific Plates (Sauber *et al.* 1994; Miller *et al.* 2001; Oskin & Iriondo 2004). Active deformation within the ECSZ was highlighted by the occurrence of the 1992  $M_w$  7.3 Landers (Massonnet *et al.* 1993; Sieh *et al.* 1993) and the 1999  $M_w$  7.1 Hector Mine (Sandwell *et al.*

2000; Fialko *et al.* 2001b; Hauksson *et al.* 2002; Simons *et al.* 2002) earthquakes.

Early InSAR observations of the Hector Mine earthquake revealed intriguing small-scale displacements along the satellite line-of-sight (LOS) on faults adjacent to the main rupture (Sandwell *et al.* 2000). These anomalous LOS displacements were later interpreted to represent the response of compliant zones (tabular volumes of reduced rigidity), to the permanent coseismic stress changes induced by the Hector Mine earthquake (Fialko *et al.* 2002). Inspection of InSAR data from the 1992 Landers, CA earthquake also revealed small-scale deformation on pre-existing faults and confirmed that this deformation is consistent with the compliant zone response to coseismic loading (Fialko 2004). Seismic probing of the Calico fault zone including trapped waves studies, and travel-time analysis of teleseismic and active source data discovered the existence of a low-velocity zone along the Calico fault coincident with the geodetically inferred compliant zone (Cochran *et al.* 2006; Cochran *et al.* 2009). Fig. 3 shows the maximum gradients of the LOS displacement residuals (track 127, frame 2907, from 1999 January 13 to 1999 October 20) computed after removing the Hector Mine earthquake coseismic model of Simons *et al.* (2002). Fig. 3 shows amplified deformation around faults located near the Hector Mine rupture. In particular, the Calico-Hidalgo (CH), the Rodman (RM), the Pinto Mountain (PM), the Homestead-Johnson Valley and the Emerson faults all exhibit some anomalous strain. Location of the seismic experiment of Cochran *et al.* (2006) is indicated with the black triangle. Some of the localized strain seen in Fig. 3 may be due to shallow creep events (outlined by dashed rectangles). For example, the localized strain south of the Pinto Mountain fault in

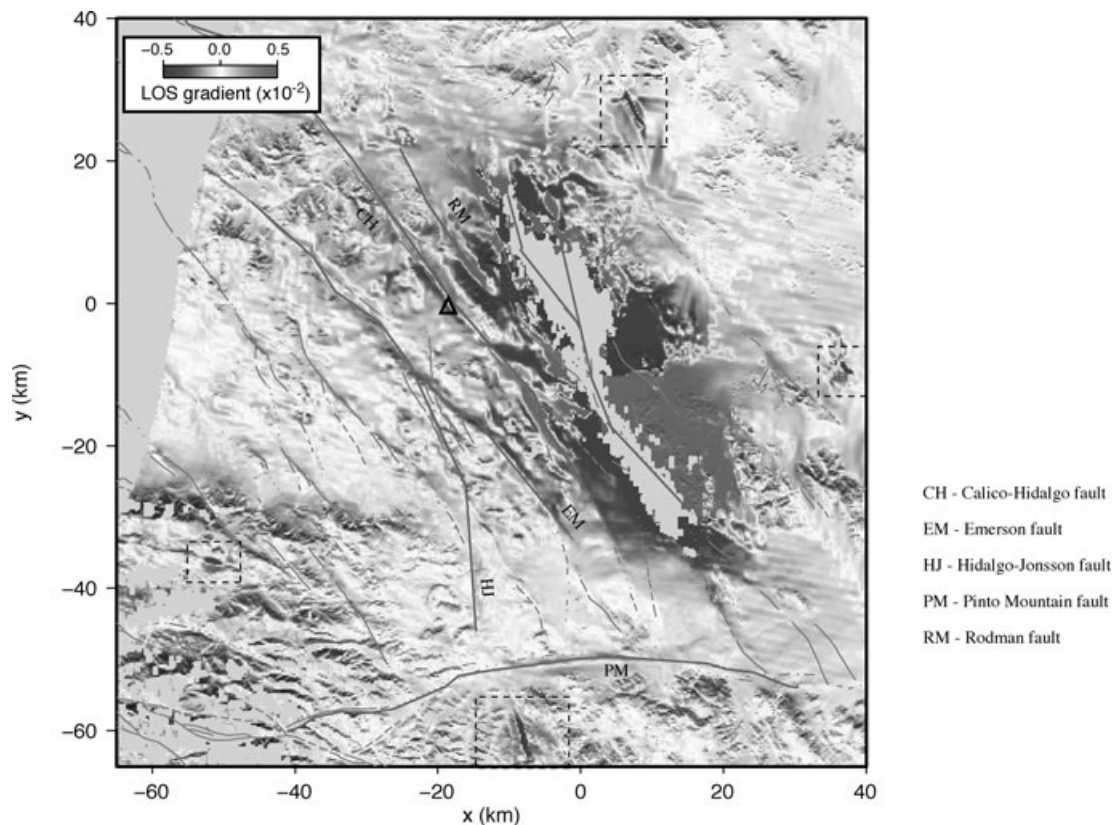


**Figure 3.** Gradient of the LOS displacement residuals after the Hector Mine coseismic model was removed. Gradient emphasizes deformation around nearby faults and underlines possible creep events (dashed quadrants). Triangle indicates location of the seismic experiment of Cochran *et al.* (2009).

the Yucca Valley occurred prior to the Hector Mine earthquake, as it is absent in interferograms that bracket the Hector Mine earthquake more tightly. This localized strain is associated with a history of seismic swarms (Jones & Helmberger 1998). The other three anomalous strain areas appear to be aseismic.

Previous studies of small-scale deformation due to faults in the ECSZ used finite element models to evaluate the coseismic response of compliant fault zones assuming a constant drop in the shear modulus and no change in the Poisson ratio within the CZ compared to the host rocks (Fialko *et al.* 2002; Fialko 2004). The fault zone response was modelled by applying coseismic stress changes inferred from the homogeneous elastic half-space solutions, and the interaction between neighbouring fault zones (e.g. around the Calico and Rodman faults) was neglected. While in general it is possible to use more sophisticated finite element simulations including multiple fault zones and realistic earthquake rupture models, such simulations require elaborate and time-consuming meshing of a computational domain, especially for non-planar and branching faults. Also, assignment of spatially variable material properties to different parts of a computational mesh is cumbersome. We use our iterative semi-analytic approach to evaluate 3-D deformation of the Earth's crust with realistic variations in elastic properties due to the presence of fault zones. We use a Poisson's solid for the 'homogenized' starting model, corresponding to the value of Poisson's ratio in the ambient crust assumed for the coseismic slip models. The modelled compliant zones (CZs) follow the geometry of the geologically mapped faults and are allowed to have across-strike, along-strike and downdip variations in the effective elastic moduli. We assume a gradual decay in the rigidity contrast away from the fault trace. The spatial variation of elastic moduli, both lateral and vertical, is parametrized with the tapered boxcar function  $\Omega_\beta$  of Barbot *et al.* (2008), with a fixed taper coefficient of  $\beta = 0.3$ . Our model includes the inferred compliant zones associated with the Calico, Rodman, Pinto Mountain, Emerson and Homestead-Johnson Valley faults in the central Mojave desert. Coseismic interferograms used to constrain the model include the 1992 April 24–August 7, ERS-1 acquisitions from the descending track 399 (Landers earthquake) and 1999 January 13–October 20, ERS-2 acquisitions from the descending track 127 (Hector Mine earthquake) (Fialko *et al.* 2002; Fialko 2004). We assume that the fault-zone properties were not affected by nearby earthquakes (but see a discussion in Hearn & Fialko (2009)).

We use the respective earthquake slip models (Simons *et al.* 2002; Fialko 2004) to remove the LOS displacements predicted for a homogeneous half-space (referred to as the homogeneous model) from the interferograms. The residual LOS displacements represent propagation artefacts (e.g. atmospheric noise), as well as the small-scale deformation such as the amplified strain due to compliant zones. Similarly, we subtract the homogeneous model from the model accounting for the presence of CZs. The residual forward model is referred to as the heterogeneous contribution (deviation of the predicted displacement field from the homogeneous elastic half-space solution). The forward models are computed on a  $512 \times 512 \times 512$  grid with a uniform node spacing of 350 m. The time involved in evaluating a single forward model is of order of five minutes on a 4-CPU shared-memory architecture computer. Fig. 4 shows the total surface displacements and the heterogeneous contribution due to the Landers and Hector Mine earthquakes, modelled with our iterative semi-analytic approach. The origin corresponds to the epicentre of the Hector Mine earthquake (116.27W, 34.595N). Profiles A–A' across the Calico and the Rodman faults, B–B' across the Calico fault, and C–C' across the Pinto Mountain fault are se-

lected because LOS displacements from these profiles are available in both the Landers and Hector Mine coseismic interferograms. For a vertical strike-slip fault, the near-field uplift is due to compression and near-field subsidence is due to extension. As one can see from Fig. 4, profile A–A' is located in the extensional quadrant of the Landers earthquake, and the compressional quadrant of the Hector Mine earthquake. Profiles B–B' and C–C' are in the compressional quadrant of the Landers earthquake, and the extensional quadrant of the Hector Mine earthquake. The fortuitous spatial configuration allows us to investigate the response of compliant fault zones to different loading conditions.

We constrain the structural and elastic properties of a compliant zone by comparing the modelled elastic contribution to the LOS data from the Landers and Hector Mine earthquakes. The model parameters include the change in Lamé parameters  $\Delta\lambda$  and  $\Delta G$ , and the compliant zone width  $W$  (fault-normal dimension) and depth  $D$  (downdip dimension). We assume that all CZs are extending vertically from the surface to a depth  $D$  and follow the strike of the corresponding fault trace at the surface. To identify the best-fitting model, we explore a range of parameters with a grid search with depths going from 2 to 18 km, width varying from 0.8 to 2.8 km and rigidity reduction ranging from  $-30$  to  $-60$  per cent compared to the ambient lithosphere. In all models, we assume a Poisson's solid for the ambient crust. The variance reduction of the Landers and Hector Mine LOS data for profiles A–A' and C–C' are shown in Fig. 5 for a range of model parameters. In these calculations, we assume that the rigidity reduction  $\Delta G$  is accompanied with a similar reduction in the other Lamé parameter  $\Delta\lambda$  or, equivalently, with a similar reduction in bulk modulus  $\Delta\kappa$ . Fig. 5(a) shows the variance reduction of profile A–A' corresponding to the Calico and Rodman CZs. Based on previous exploration, we assume that the thickness of the Rodman CZ is half that of the Calico CZ. The lesser depth extent of the Rodman CZ is required by the small wavelength of the corresponding LOS data, most visible in the Landers earthquake data (see Fig. 6a). The variance reduction is systematically better for the Hector Mine data, due to a better signal-to-noise ratio in the Hector Mine radar interferogram. Residuals are larger for CZs with a small rigidity contrast, the best variance reduction being obtained with the large reduction  $\Delta G = -60$  per cent. For all the rigidity contrasts considered, the required width of the Calico CZ for both the Landers and the Hector Mine data lies in the range  $W = 4$ – $5$  km. The preferred thickness of the Calico CZ is slightly (about 20 per cent) higher for the Landers than for the Hector Mine data. Our preferred model for the compliant zone surrounding the Calico fault, north of Galway Dry Lake, explaining both the Landers and Hector Mine data simultaneously, implies a 60 per cent shear and bulk moduli reduction, a depth of  $4 \pm 0.5$  km and a  $2.0 \pm 0.2$  km width. Best model for the Rodman CZ is similar, except for a 2 km depth. We performed additional simulations, considering an increase in Poisson's ratio in the compliant zone. The best variance reduction was obtained for a shallower structure. However, all models with increased Poisson's ratio led to higher misfit with both Landers and Hector Mine LOS data. These results indicate that a change in the CZ bulk modulus accompanying the reduction in rigidity is a robust feature required by the radar data.

Fig. 5(b) shows the variance reduction of profile C–C' corresponding to the Pinto Mountain compliant zone. As in case of models shown in Fig. 5(a), we assume that rocks in the fault zone behave as a Poisson's solid, so that Poisson's ratio is constant and equals 0.25. For small rigidity contrasts ( $-\Delta G = 30$ – $40$  per cent), the LOS data provide essentially a lower bound on the inferred width  $W = 2.0 \pm 0.1$  km and depth  $D = 9$  km of the Pinto Mountain CZ.

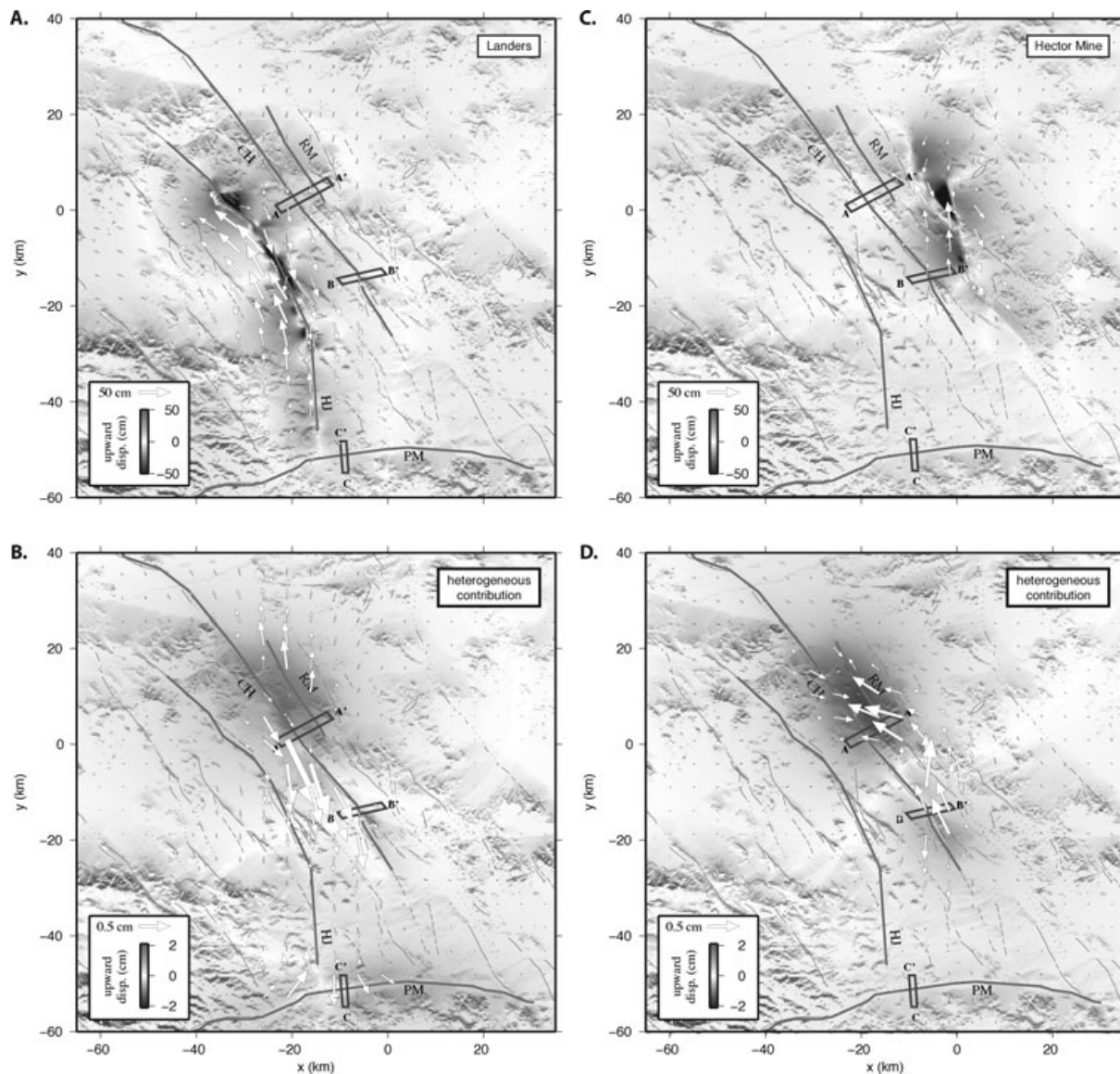


**Figure 4.** (a) Map view of surface displacement corresponding to full 3-D deformation in a heterogeneous crust due to the 1992 Landers, CA earthquake. Vectors and colour scale indicate horizontal and vertical displacements, respectively and uplift is taken to be positive. (b) Elastic structure contribution corresponding to the Landers model. (c) Model of the total surface displacements due to the Hector Mine earthquake. (d) Hector Mine elastic structure contribution. The deformation is localized around CZs: the Calico-Hidalgo (CH), the Rodman (RM) and the Pinto Mountain (PM) faults exhibit amplified strain. Profiles A–A', B–B' and C–C' are shown in subsequent figures. Origin corresponds to the epicentre of the Hector Mine earthquake (116.27W, 34.595N). Light grey lines correspond to identified faults in the ECSZ and darker grey lines indicate modelled compliant zones (CZ).

There is an apparent trade-off between the required width and the rigidity reduction, most apparent for the Landers data. However, the best variance reduction is obtained for models with the largest rigidity reduction. For elastic contrasts larger than  $\Delta G = -45$  per cent the width required by the Landers and Hector Mine data differ by more than 15 per cent and the models using the preferred width inferred from the Hector Mine data produce only a poor fit to the Landers LOS data. Our preferred model, which we indicate by a circle in Fig. 5, lies within 2 per cent variance reduction of the independent best-fitting models for Landers and Hector Mine. Our preferred model, fitting both the Landers and Hector Mine data simultaneously, implies a 45 per cent reduction in both shear and bulk moduli in a zone 1.75 km wide and at least 9 km deep surrounding the Pinto Mountain fault. The minimum depth of 9 km for the Pinto Mountain CZ is a robust feature that is required by both data sets.

Fig. 6(a) shows the observed and modelled LOS displacements along profile A–A'. Profile A–A' crosses over the Calico and the Rodman faults, north of Galway Dry Lake, close to the seismic tomography experiment of Cochran *et al.* (2009) (see Fig. 3). There is little correlation between topography (dashed line) and the InSAR data, indicating that the observed variations in the LOS displacements do not result from atmospheric phase delays. We also note the change in polarity in the LOS displacements corresponding to the Hector Mine and Landers coseismic interferograms. This change in polarity is an expected signature of the vertical displacement due to a compliant zone, given a reversal in sign of the fault-normal coseismic stress change. The assumed location and thickness of the Calico and Rodman compliant zones are indicated in Fig. 6(a) by grey bands. Solid lines in Fig. 6(a) represent deformation due to our preferred fault zone model, sampled along the respective profiles.

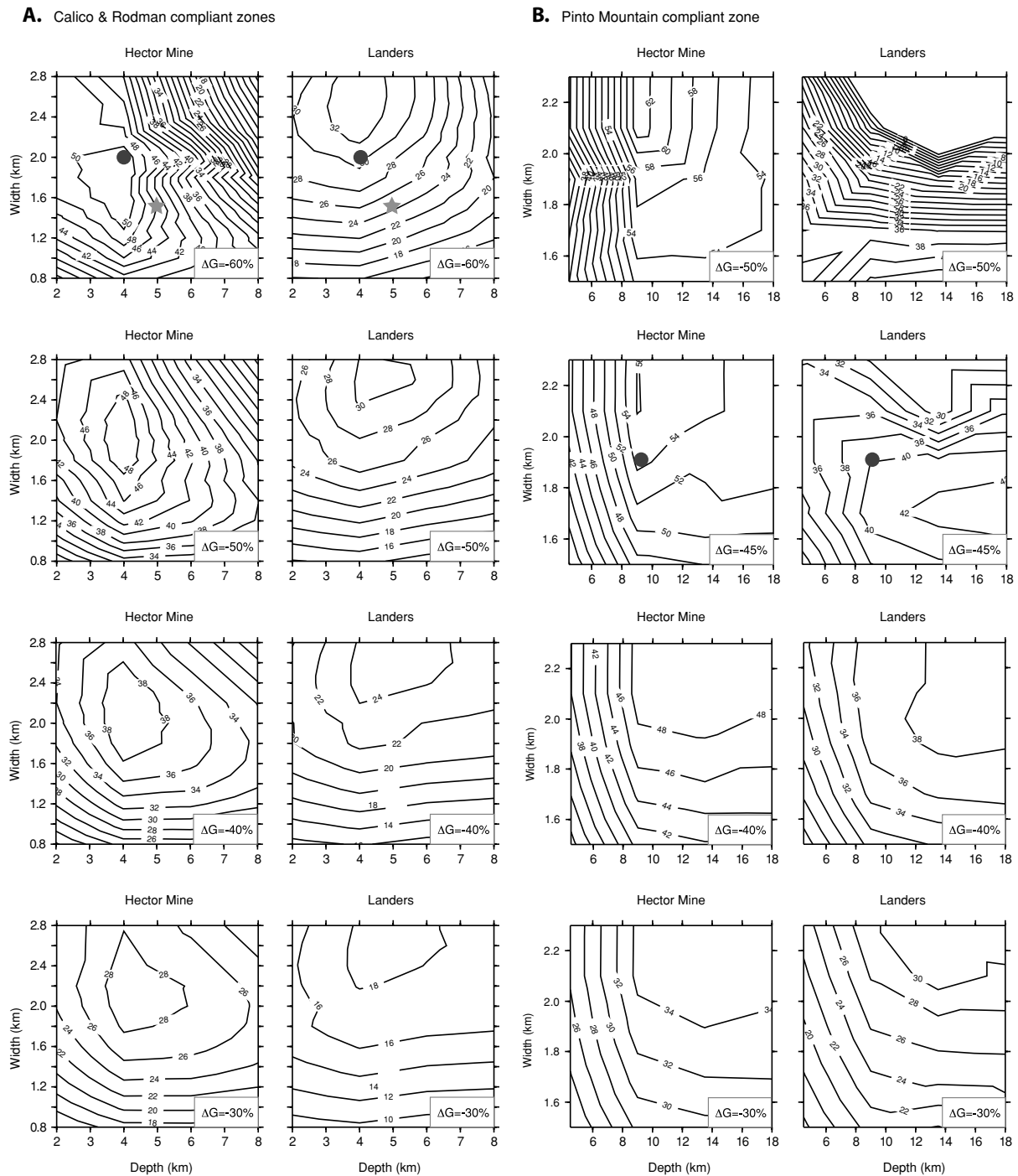


**Figure 5.** Exploration of the CZ model space. Variance reduction of the Landers and Hector Mine LOS data for the (a) Calico/Rodman and (b) the Pinto Mountain profiles (transects A–A' and C–C', respectively, in Fig. 4) as a function of the CZ width, depth and rigidity reduction  $\Delta G$ . All models assume a Poisson's solid ( $\nu = 0.25$ ) in the ambient crust and in the CZ. The star symbol indicates the preferred model of Cochran *et al.* (2008) corresponding to a 36 per cent reduction in  $P$ -wave velocity. The circle indicates our preferred model, based on fitting the Landers and Hector Mine LOS data simultaneously.

The modelled LOS displacements account for range variations in the radar incidence angle. Results shown in Fig. 6(a) accurately simulate the 3-D response of closely spaced compliant zones due to the Calico and Rodman faults to coseismic loading, and represent a substantial improvement over the previously published simplified models (e.g. Fialko *et al.* 2002). Our preferred model for the compliant zone surrounding the Calico fault, north of Galway Dry Lake, implies a 60 per cent reduction in shear modulus and no change in

the Poisson's ratio (accompanied by a 60 per cent reduction in the value of the bulk modulus) compared to ambient rocks, in a finite zone 4 km deep and 2.0 km wide. Our preferred model for the CZ due to the Rodman fault implies the same elastic moduli reduction, but to a shallower depth of  $D = 2.0$  km.

Fig. 6(b) shows the observed and modelled LOS displacements along profile B–B' in Fig. 4. InSAR data and models are shown for both the Landers and the Hector Mine earthquakes.

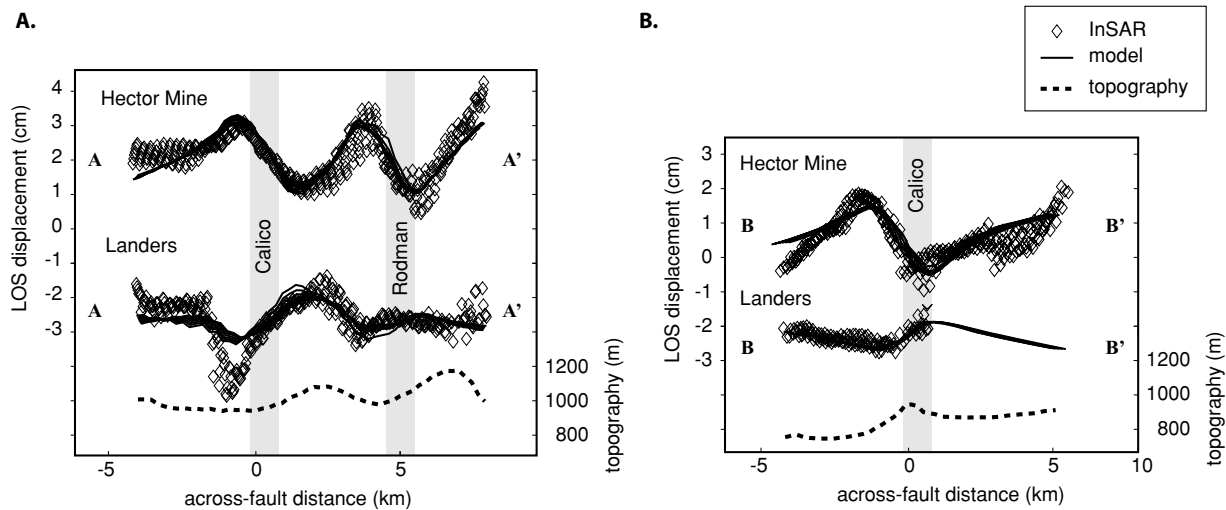


**Figure 6.** (a) Observed (diamond) and modelled (solid line) LOS displacements from profile A–A' corresponding to the Landers (bottom) and Hector Mine (top) coseismic interferograms North of Galway Dry Lake. The Calico model corresponds to a 4 km deep, 2.0-km-wide structure with a 60 per cent rigidity reduction, as indicated by a circle in Fig. 5(a). The Rodman model is similar except for a shallow structure of 2 km. (b) Observed and modelled LOS residual displacements across a southern segment of the Calico fault (profile B–B'). At this location, the Calico model implies a shallow (2–3 km) structure 1.8 km wide with 45–50 per cent rigidity reduction. Topography (dashed line) does not correlate with InSAR phase delay, indicating a limited tropostatic noise contribution. The continuous profiles correspond to forward models from several closely spaced parallel profiles within boxes outlined in Fig. 4. The flip of polarity between the Landers and Hector Mine coseismic InSAR data is an expected signature of a compliant zone.

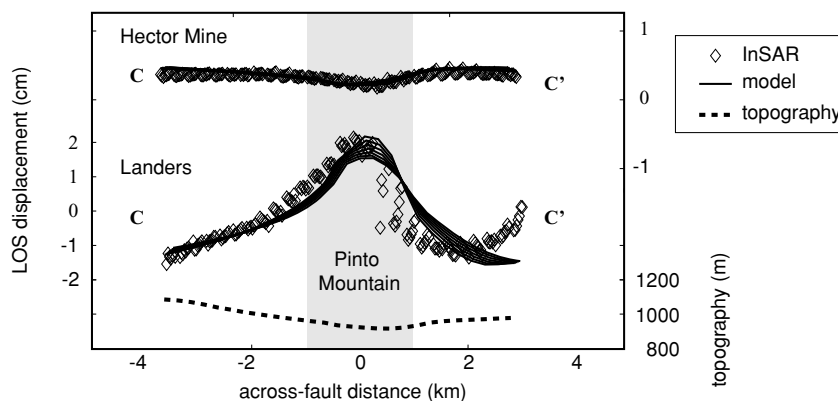


**Figure 7.** Modelled (solid line) and observed (diamonds) LOS displacements across the Pinto Mountain fault, profile C–C'. The predictions correspond to a single compliant zone model with a 45 per cent reduction in both shear and bulk moduli, indicated by a circle in Fig. 5(b). The CZ structure is 1.75 km wide and at least 9 km deep. The continuous profiles correspond to several closely spaced parallel profiles from the forward model and indicate the variation of deformation within the C–C' box outlined in Fig. 4. Note the separate scale for the Hector Mine data and forward model.

Topography profile exhibits a ridge close to the location of the assumed compliant zone but LOS displacements corresponding to the two seismic events change polarity and are not well correlated with topography, suggesting that the observed LOS displacements are not an atmospheric artefact. Incomplete data for the Landers earthquake, east of the compliant zone is due to limited coverage of the available satellite track 399. InSAR data for the Landers earthquake are nevertheless sufficient to suggest a localized increase in LOS displacements centred on the Calico fault trace. Profile B–B' samples a segment of the Calico fault located to the South of Galway Dry Lake, about 35 km south of profile A–A'. This portion of the Calico fault was subjected to compression during the Landers earthquake and extension during the Hector Mine earthquake, coincident with the observed polarity of vertical displacement in Fig. 4. Our preferred CZ model indicates a reduction of 45–50 per cent in shear and bulk moduli in a 1.8-km-wide zone extending from the surface to a depth of 2–3 km. The CZ model can explain data

from both the Hector Mine and Landers earthquakes. Reductions in the effective elastic moduli on the southern segment of the Calico fault are inferred to be somewhat smaller compared to those on the northern segment. This result highlights a possibility of substantial variations in effective elastic properties along the same fault zone. A 10 per cent along-strike variation in elastic moduli compared to surrounding rocks was also inferred along the Johnson Valley and the Kickapoo faults, the southern segments of the Landers rupture (Li *et al.* 2000).

Fig. 7 shows the modelled and the observed LOS displacements across the Pinto Mountain fault due to the Landers and Hector Mine earthquakes (profile C–C' in Fig. 4). Profile C–C' is located to the east of the Landers rupture, in a compressional quadrant near the southern tip of the rupture. This proximity likely explains a relatively large (up to 30 mm) LOS displacement due to the compliant zone of the Pinto Mountain fault. The southern tip of the Hector Mine rupture is located further away, about 80 km to the

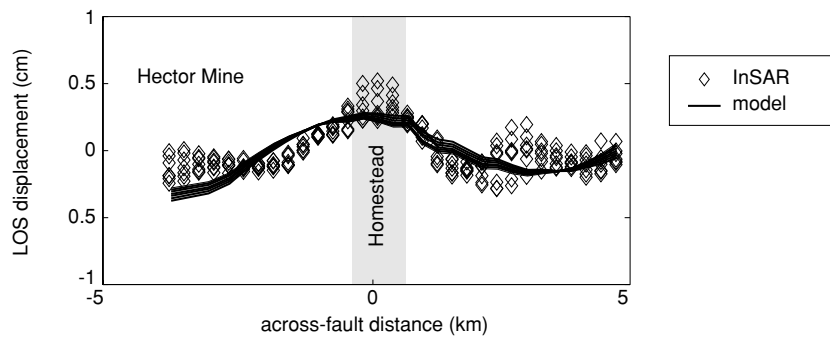


**Figure 8.** Modelled (solid line) and observed (diamonds) LOS displacements across the Homestead fault. Forward model corresponds to a compliant zone with a 50 per cent reduction in shear and bulk moduli in a block 4–5 km deep and 1.5 km wide. The continuous profiles correspond to forward models from several closely spaced parallel profiles within boxes outlined in Fig. 4.

north-northeast. Both the larger distance to, and the smaller size of the Hector Mine earthquake imply smaller stress perturbation on the Pinto Mountain fault, and explain the reduced amplitude of the coseismic LOS displacements, compared to those from the Landers event. Similar to the observed deformation patterns on the Calico and Rodman faults, the polarity of LOS displacements on the Pinto Mountain fault is different for the Landers and Hector Mine events, consistent with coseismic stress changes. Our preferred model for the Pinto Mountain compliant zone, as indicated by a circle in Fig. 5, has width of 1.9 km, a depth of at least 9 km, a 50 per cent reduction in shear modulus and no change in Poisson's ratio compared to ambient crust. The deeper compliant zone compared to neighbouring Calico and Rodman is required by the large wavelength of the LOS displacements.

Fig. 8 shows the modelled and the observed LOS displacements across the Homestead fault due to the Hector Mine earthquake. The LOS displacements can be explained by the presence of a CZ about 1.5 km wide, extending from the surface to a depth of 4–5 km with 50 per cent reduction in shear modulus, and the same Poisson's ratio as in ambient rocks. A model assuming a CZ around the Homestead fault shows a good agreement with the InSAR data. Unfortunately, no data exist for the 1992 Landers earthquake due to decorrelation in the near field of the rupture.

#### 4 DISCUSSION

Our analysis of space geodetic observations in the ECSZ using fully 3-D models lends support to previous inferences of long-lived compliant zones around major faults, with appreciable reductions in the effective shear and bulk moduli. Our inferred width of compliant zones is 2.0 km for the Calico and the Rodman process zones and 1.9 km for the Pinto Mountain fault. Over the past two decades, the structure of fault zones has been primarily investigated using fault zone trapped waves generated by earthquakes or explosions. For example, the Karadere-Duzce fault zone, a secondary branch of the North Anatolian Fault, is inferred to have a wave-trapping structure  $\sim 100$  m wide, with a velocity decrease of about 50 per cent compared to the surrounding rocks (Ben-Zion *et al.* 2003). Trapped waves generated by aftershocks following the 1992 Landers earthquake are best explained by a 250-m-wide low velocity zone in the southern segment of the rupture, that tapers to 100–150 m at 8.2 km depth (Li *et al.* 2000). Trapped-wave studies rely on seismic sources within compliant zones (most commonly, aftershocks) to detect and quantify the elastic contrasts (Li & Leary 1990; Li *et al.* 1998a,b, 1999, 2000; Ben-Zion *et al.* 2003). The

strength of the low-velocity anomalies is believed to vary over the earthquake cycle (Marone *et al.* 1995; Li *et al.* 1998a; Vidale & Li 2003), but it is still unclear if results from seismic studies are directly applicable to the longer geodetic timescale, due to the frequency dependence of elastic moduli. In this study, we investigated major faults that did not rupture in historic times and therefore are well within the interseismic phase of the earthquake cycle. Our preferred models suggest considerably (in case of the Pinto Mountain fault—an order of magnitude) larger fault zone width compared to most previous seismic studies of other faults. However, a recent seismic tomography and trapped wave experiment on the Calico fault (Cochran *et al.* 2009) confirms our interpretation and provides a direct independent evidence for the existence of a massive long-lived compliant fault zone along the Calico fault. Our preferred model of the Calico compliant zone, with a 4 km depth and 2.0 km width is very similar to the results of (Cochran *et al.* 2009) which imply a fault zone 1–2 km wide,  $\sim 5$  km deep, with a rigidity reduction of 50–75 per cent. Our interpretation of InSAR data from the Pinto Mountain fault suggests that a compliant zone extends from the surface to a depth of at least 9 km, that is, through much of the brittle seismogenic layer.

Our models of compliant zones along major strike-slip faults in the ECSZ require a significant reduction in the effective shear modulus. A robust feature of InSAR observations is the change in polarity of the LOS displacements within several fault zones due to the Landers and Hector Mine earthquakes. The observed change in polarity is primarily due to the vertical displacements within the compliant zone. The polarity of vertical motion is well constrained by InSAR observation and our results suggest that a reduction in both shear and bulk moduli better describes the variations in the effective elastic moduli within the compliant zones surrounding active faults in the ECSZ. These results contrast with the assumptions of theoretical models of fault damage in which the latter is related to changes in the shear modulus alone (Lyakhovskiy *et al.* 2001; Hamiel *et al.* 2004). Hearn & Fialko (2009) have investigated the response of compliant zones in the ECSZ due to both a permanent elastic moduli reduction in the fault process zones and a 2 per cent coseismic change in rigidity in the same structure motivated by findings of Vidale & Li (2003). The conclusion of Hearn & Fialko (2009) is that it is difficult to fit the data in the presence of coseismic softening of the fault zones, unless the fault zone material is nearly incompressible. This study suggests that the data can be well explained by permanent compliant zones with normal Poisson's ratios, this highlighting the need for accurate monitoring of changes in the fault-zone rigidity due to nearby earthquakes.

## 5 CONCLUSIONS

We have presented an iterative approach to model 3-D deformation due to faults in a heterogeneous elastic half-space. The decomposition of the elastic moduli into a constant part and a spatially varying part allows us to formulate an iterative solution that takes advantage of the Green function for a homogeneous medium. Spatial variations in elastic properties are accounted for by equivalent body forces and equivalent surface traction. This approach obviates the need for deriving or numerically calculating the specific Green function in case of heterogeneous elastic structures. It allows one to readily evaluate the effect of spatial variations in elastic properties on deformation in the surrounding medium.

A possible drawback of our iterative approach is a potentially large number of SA required to accurately evaluate the heterogeneous elastic response. Likewise, the numerical estimation of the convolution between the homogeneous Green function and the equivalent body forces—typically scaling as  $N^2$ , where  $N$  is the number of nodes—can be expensive as the equivalent body forces representing the effect of elastic variations in the homogenized medium can occupy large domains. Our approach consists in evaluating the deformation numerically in the Fourier domain. We use the semi-analytic Green function for a half-space to compute the displacement field due to the presence of arbitrarily distributed body forces in the computational domain. Free-surface boundary condition is enforced by counterbalancing the stress field on the surface plane obtained first from the whole space solution. The half-space solution is finally obtained by application of analytic solutions, in the Fourier domain, for some normal and tangential traction applied at the surface (the so-called Boussinesq's and Cerruti's problems). The computational burden associated with a Fourier domain solution is independent of the spatial extent or distribution of the body forces. The use of fast Fourier transforms allows us to compute multiple SAs efficiently. One iteration on a  $512 \times 512 \times 512$  computation grid takes about a minute on a 4-CPU machine with a shared memory architecture. Typically, about 10 iterations are needed to reach convergence. In most cases, the proposed numerical method is a practical alternative to more advanced models like finite elements because it does not require elaborate and time-consuming meshing of a computational domain, especially for non-planar and branching faults. Also, the assignment of spatially variable material properties to different parts of a computational mesh is straightforward, due to the uniform sampling of the computation domain.

We compared our numerical results with analytic and semi-analytic solutions for antiplane, plane-strain and 3-D deformation problems. We find that our numerical solutions for antiplane problems fall within 5 per cent of analytical solutions, even in the case of large contrasts in elastic properties. In the case of plane strain symmetry, we compared our solution to results of the propagator method (P. Segall, personal communication, 2008). We use the semi-analytic Green function approach of Wang *et al.* (2003) and finite element calculations to validate our approach in 3-D for vertical and lateral variations in elastic moduli. Accuracy is better than about 5 per cent of the expected elastic structure contribution for elastic contrasts lower than 50 per cent and better than about 10 per cent for contrasts higher than 50 per cent compared to homogenized values. We conclude that our semi-analytic method provides a sufficient accuracy to model realistic problems of 3-D deformation in a heterogeneous crust. We applied this method to investigate the structure and properties of compliant damage zones associated with young active faults in the ECSZ. We modelled the LOS displacements documented by radar interferometry during the 1992 Landers

and the 1999 Hector Mine earthquakes (Fialko *et al.* 2002; Fialko 2004). We model the inferred compliant zones by a gradual reduction in rigidity and bulk modulus around the geologically mapped fault trace. Using a grid search, we explored a range of parameters that can explain simultaneously LOS displacements from both the Landers and Hector Mine earthquakes.

The InSAR data near the Calico and the Rodman faults, respectively, are best explained by the presence of a compliant zone that extends from the surface to a depth of 4 and 2 km, respectively, with a rigidity reduction of 60 per cent compared to ambient rocks. No contrast in the Poisson ratio is inferred between the host rocks and the Calico fault zone. The wavelength of LOS displacements around the Calico and the Rodman faults require an effective compliant zone width of about 2.0 km. One segment of the Calico fault, South of Galway Dry Lake is partially sampled by both Hector Mine and Landers interferograms. Data corresponding to this southern segment is best modelled with a 45–50 per cent reduction in shear and bulk moduli in a 2–3 km deep, 1.8 km wide structure. Our modelling results show substantial along-strike variations in the elastic properties and fault zone size for the Calico fault. InSAR data around the Pinto Mountain fault are best modelled with a compliant zone that extends from the surface to a least 9 km depth, in a 1.75-km-wide zone with a 45 per cent reduction in effective shear and bulk moduli. A single elastic model of a heterogeneous crust with lateral variations around the Calico, the Rodman and the Pinto Mountain faults can explain the InSAR data of both Landers and Hector Mine earthquakes. We conclude that the presence of compliant zones around the Calico, the Rodman and the Pinto Mountain faults in the ECSZ is a robust feature of these InSAR observations. The anomalous LOS displacements observed in the Hector Mine and Landers interferograms correspond to the elastostatic response of a laterally heterogeneous crust in the east California shear zone. The residual LOS displacements in the Hector Mine InSAR data around the Homestead-Johnson Valley can be explained by the presence of a compliant zone with a 50 per cent reduction in shear and bulk moduli in a block 4–5 km deep and 1.5 km wide. Inferred elastic properties in the Homestead Valley process zone indicates that the northernmost fault segments of the 1999 Landers earthquake ruptured in the middle of a compliant zone.

Our modelling results indicate that damage accumulation around active faults is accompanied by a reduction in both shear and bulk effective moduli with a relatively small increase in Poisson's ratio. The 'conserved Poisson's ratio' end-member scenario seems to be more applicable to the ECSZ than the 'conserved bulk-modulus' end-member. These observations suggest pervasive and widespread damage around active crustal faults. The inferred properties of compliant zones may be used to quantify the amount of damage experienced by the host rocks throughout the fault history.

## ACKNOWLEDGMENTS

We thank Jill Pearse for her help with finite element calculations. Finite element meshes were generated using the pre-processor AP-MODEL written by Shelly Kenner. The manuscript benefited from comments by the Editor Thorsten Becker, and thorough reviews by Kaj Johnson and an anonymous reviewer. A numerical code used in this paper is available at <http://sylvain.barbot.free.fr/crust/>. This work was supported by the National Science Foundation (grant EAR-0450035) and the Southern California Earthquake Center (the SCEC contribution number for this paper is 1266). SAR data used

in this study are copyright of the European Space Agency, made available via the WInSAR Consortium at UNAVCO.

## REFERENCES

- Aki, K. & Richards, P.G., 1980. *Quantitative Seismology*, Vol. I, W.H. Freeman and Company, New York.
- Ambraseys, N., 1970. Some characteristic features of the North Anatolian fault zone, *Tectonophysics*, **9**, 143–165.
- Backus, G. & Mulcahy, M., 1976a. Moment tensors and other phenomenological descriptions of seismic sources—I. Continuous displacements, *Geophys. J. R. astr. Soc.*, **46**, 341–361.
- Backus, G. & Mulcahy, M., 1976b. Moment tensors and other phenomenological descriptions of seismic sources—II. Discontinuous displacements, *Geophys. J. R. astr. Soc.*, **47**, 301–329.
- Barbot, S., Fialko, Y. & Sandwell, D., 2008. Effect of a compliant fault zone on the inferred earthquake slip distribution, *J. geophys. Res.*, **113**, B06404, doi:10.1029/2007JB005256.
- Barbot, S., Fialko, Y. & Bock, Y., 2009. Postseismic deformation due to the Mw 6.0 2004 parkfield earthquake: stress-driven creep on a fault with spatially variable rate-and-state friction parameters, *J. geophys. Res.*, in press, doi:10.1029/2008JB005748.
- Ben-Zion, Y. *et al.*, 2003. A shallow fault-zone structure illuminated by trapped waves in the Karadere-Duzce branch of the North Anatolian Fault, western Turkey, *Geophys. J. Int.*, **152**, 699–699.
- Bender, C.M. & Orszag, S.A., 1978. *Advanced Mathematical Methods for Scientists and Engineers*, McGraw-Hill, New York.
- Bracewell, R., 2003. *The Fourier Transform and its Applications, Electrical and Computer Engineering*, 3rd edn, Tata McGraw-Hill, New York.
- Brown, C.M., Dreyer, W. & Müller, W.H., 2003. The convergence of a DFT-algorithm for solution of stress-strain problems in composite mechanics, *J. Eng. Math. Tech.*, **125**, 27–37.
- Burridge, R. & Knopoff, L., 1964. Body force equivalents for seismic dislocations, *Bull. seism. Soc. Am.*, **54**(6), 1875–1888.
- Chen, Q. & Freymueller, J., 2002. Geodetic evidence for a near-fault compliant zone along the San Andreas fault in the San Francisco Bay area, *Bull. seism. Soc. Am.*, **92**, 656–671.
- Chester, J.S., Chester, F.M. & Kronenberg, A.K., 2005. Fracture surface energy of the Punchbowl fault, San Andreas system, *Nature*, **437**, 133–136.
- Cochran, E.S., Radiguet, M., Shearer, P.M., Li, Y.-G., Fialko, Y. & Vidale, J.E., 2006. Seismic imaging of the damage zone around the Calico Fault, *EOS, Trans. Am. geophys. Un.*, **87**(52).
- Cochran, Y., Li, Y.-G., Shearer, P., Barbot, S., Fialko, Y. & Vidale, J., 2009. Seismic and geodetic evidence for extensive, long-lived fault damage zones, *Geology*, **37**(4), 315–318.
- Delves, L. & Mohamed, J., 1985. *Computational Methods for Integral Equations*, Cambridge Univ. Press, New York, 373 pp.
- Dieterich, J. & Smith, D.E., 2007. Rate-state modeling of stress relaxation in geometrically complex fault systems, *EOS, Trans. Am. geophys. Un.*, **88**(52), *Fall Meet. Suppl.*, pp. abstract S13B–1308.
- Dokka, R.K. & Travis, C.J., 1990a. Late cenozoic strike-slip faulting in the Mojave Desert, California, *Tectonics*, **9**(2), 311–340.
- Dokka, R.K. & Travis, C.J., 1990b. Role of the Eastern California Shear Zone in accommodation Pacific-North American plate motion, *Geophys. Res. Lett.*, **17**(9), 1223–1226.
- Du, Y., Segall, P. & Gao, H., 1994. Dislocations in inhomogeneous media via a moduli perturbation approach: general formulation and two-dimensional solutions, *J. geophys. Res.*, **99**(B7), 13 767–13 779.
- Du, Y., Segall, P. & Gao, H., 1997. Quasi-static dislocations in three-dimensional inhomogeneous media, *Geophys. Res. Lett.*, **24**(18), 2347–2350.
- Eshelby, J.D., 1957. The determination of the elastic field of an ellipsoidal inclusion, and related problems, *Proc. R. Soc. Lond. A*, **241**(1226), 376–396.
- Farid, H. & Simoncelli, E., 2004. Differentiation of discrete multidimensional signals, *IEEE Trans. Im. Proc.*, **13**(4), 496–508.
- Fialko, Y., 2004. Probing the mechanical properties of seismically active crust with space geodesy: study of the co-seismic deformation due to the 1992  $M_w$  7.3 Landers (Southern California) earthquake, *J. geophys. Res.*, **109**, B03307, doi:10.1029/2003JB002756.
- Fialko, Y., 2007. Fracture and frictional mechanics—theory, in *Treatise on Geophysics*, Vol. 4, pp. 83–106, ed. Schubert, G., Elsevier Ltd., Oxford.
- Fialko, Y., Khazan, Y. & Simons, M., 2001a. Deformation due to a pressurized horizontal circular crack in an elastic half-space, with applications to volcano geodesy, *Geophys. J. Int.*, **146**, 181–190.
- Fialko, Y., Simons, M. & Agnew, D., 2001b. The complete (3-D) surface displacement field in the epicentral area of the 1999  $M_w$  7.1 Hector Mine earthquake, southern California, from space geodetic observations, *Geophys. Res. Lett.*, **28**, 3063–3066.
- Fialko, Y., Sandwell, D., Agnew, D., Simons, M., Shearer, P. & Minster, B., 2002. Deformation on nearby faults induced by the 1999 Hector Mine earthquake, *Science*, **297**, 1858–1862.
- Gable, C.W., O’Connell, R.J. & Travis, B.J., 1991. Convection in three dimensions with surface plates: generation of toroidal flow, *J. geophys. Res.*, **96**(B5), 8391–8405.
- Golub, G.H. & Van Loan, C.F., 1996. *Iterative Methods for Linear Systems, Matrix Computations*, 3rd edn, Johns Hopkins Univ. Press, Baltimore, MD.
- Hamiel, Y. & Fialko, Y., 2007. Structure and mechanical properties of faults in the North Anatolian Fault system from InSAR observations of coseismic deformation due to the 1999 Izmit (Turkey) earthquake, *J. geophys. Res.*, **112**, B07412, doi:10.1029/2006JB004777.
- Hamiel, Y., Liu, Y., Lyakhovskiy, V., Ben-Zion, Y. & Lockner, D., 2004. A visco-elastic damage model with applications to stable and unstable fracturing, *Geophys. J. Int.*, **159**, 1155–1165.
- Hauksson, E., Jones, L. & Hutton, K., 2002. The 1999  $M_w$  7.1 Hector Mine, California, earthquake sequence: complex conjugate strike-slip faulting, *Bull. seism. Soc. Am.*, **92**, 1154–1170.
- Hearn, E.H. & Fialko, Y., 2009. Can compliant fault zones be used to measure absolute stresses in the upper crust? *J. geophys. Res.*, **114**, B04403, doi:10.1029/2008JB005901.
- Hill, R., 1965. A self-consistent mechanics of composite materials, *J. Mech. Phys. Solids*, **13**, 213–222.
- Jones, L.E. & Helmberger, D.V., 1998. Earthquake source parameters and fault kinematics in the Eastern California Shear Zone, *Bull. seism. Soc. Am.*, **88**(6), 1337–1352.
- Kachanov, L., 1986. *Introduction to Continuum Damage Mechanics*, Martinus Nijhoff, Dordrecht.
- Kato, T., 1980. *Perturbation Theory for Linear Operators*, Springer-Verlag, New York.
- Lebensohn, R.A., 2001. N-site modelling of a 3D viscoplastic polycrystal using the fast Fourier transform, *Acta Mater*, **49**, 2723–2737.
- Li, Y., Vidale, J., Aki, K., Marone, C. & Lee, W., 1994. Fine-structure of the Landers fault zone—segmentation and the rupture process, *Science*, **265**, 367–370.
- Li, Y., Aki, K., Vidale, J. & Alvarez, M., 1998a. A delineation of the Nojima fault ruptured in the M7.2 Kobe, Japan, earthquake of 1995 using fault zone trapped waves, *J. geophys. Res.*, **103**(B4), 7247–7263.
- Li, Y., Vidale, J., Aki, K., Xu, F. & Burdette, T., 1998b. Evidence of shallow fault zone strengthening after the 1992 M7.5 Landers, California, earthquake, *Science*, **279**, 217–219.
- Li, Y., Aki, K., Vidale, J. & Xu, F., 1999. Shallow structure of the landers fault zone from explosion-generated trapped waves, *J. geophys. Res.*, **104**, 20 257–20 275.
- Li, Y., Vidale, J., Aki, K. & Xu, F., 2000. Depth-dependent structure of the Landers fault zone from trapped waves generated by aftershocks, *J. geophys. Res.*, **105**, 6237–6254.
- Li, Y.G. & Leary, P.C., 1990. Fault zone trapped seismic waves, *Bull. seism. Soc. Am.*, **80**, 1245–1271.
- Liu, J., Sieh, K. & Hauksson, E., 2003. A structural interpretation of the aftershock “Cloud” of the 1992  $M_w$  7.3 Landers earthquake, *Bull. seism. Soc. Am.*, **93**, 1333–1344.

- Love, A.E.H., 1927. *A Treatise on the Mathematical Theory of Elasticity*, Cambridge University Press, Cambridge (Reprinted in 1944 by Dover Publications, New York).
- Lyakhovskiy, V., Ben-Zion, Y. & Agnon, A., 2001. Earthquake cycle, fault zones, and seismicity patterns in a rheologically layered lithosphere, *J. geophys. Res.*, **106**, 4103–4120.
- Malvern, L.E., 1969. *Introduction to the Mechanics of a Continuum Medium*, Prentice-Hall, Englewood Cliffs, NJ, 713 pp.
- Manighetti, I., King, G., Gaudemer, Y., Scholz, C. & Doubre, C., 2001. Slip accumulation and lateral propagation of active normal faults in Afar, *J. geophys. Res.*, **106**, 13 667–13 696.
- Marone, C., Vidale, J.E. & Ellsworth, W., 1995. Fault healing inferred from the time dependent variations in source properties of repeating earthquakes, *Geophys. Res. Lett.*, **22**, 3095–3098.
- Massonnet, D., Rossi, M., Carmona, C., Adragna, F., Peltzer, G., Feigl, K. & Rabaute, T., 1993. The displacement field of the Landers earthquake mapped by radar interferometry, *Nature*, **364**, 138–142.
- McClellan, J., Parks, T. & Rabiner, L., 1973. A computer program for designing optimum FIR linear phase digital filters, *Audio Electroacoustics, IEEE Trans.*, **21**(6), 506–526.
- Miller, M.M., Johnson, D.J., Dixon, T.H. & Dokka, R.K., 2001. Refined kinematics of the Eastern California shear zone from GPS observations, 1993–1998, *J. geophys. Res.*, **106**(B2), 2245–2264.
- Mindlin, R.D., 1936. Force at a point in the interior of a semi-infinite solid, *J. Appl. Phys.*, **7**, 195–202.
- Moulinec, H. & Suquet, P., 1998. A numerical method for computing the overall response of nonlinear composites with complex microstructure, *Comp. Meth. App. Mech. Eng.*, **157**, 69–94.
- Nemat-Nasser, S., 2004. *Plasticity. A Treatise on Finite Deformation of Heterogeneous Inelastic Materials*, Cambridge Monographs on Mechanics, Cambridge University Press, Cambridge.
- Nemat-Nasser, S. & Hori, M., 1999. *Micromechanics: Overall Properties of Heterogeneous Materials*, 2nd edn, Elsevier, Amsterdam.
- Niazy, A., 1975. An exact solution for a finite, two-dimensional moving dislocation in an elastic half-space with application to the San Fernando earthquake of 1971, *Bull. seism. Soc. Am.*, **65**(6), 1797–1826.
- Oskin, M. & Iriondo, A., 2004. Large-magnitude transient strain accumulation on the Blackwater fault, Eastern California shear zone, *Geology*, **32**, 313–316.
- Pollitz, F.F., 2003. Post-seismic relaxation theory on a laterally heterogeneous viscoelastic model, *Geophys. J. Int.*, **155**, 55–78.
- Press, W.H., Teukolsky, S.A., Vetterling, W.T. & Flannery, B.P., 1992. *Numerical Recipes in C: The Art of Scientific Computing*, 2nd edn, Cambridge Univ. Press, New York, 994 pp.
- Rice, J.R., Sammis, C.G. & Parsons, R., 2005. Off-fault secondary failure induced by a dynamic slip pulse, *Bull. seism. Soc. Am.*, **95**, 109–134.
- Rybicki, K., 1971. The elastic residual field of a very long strike-slip fault in the presence of a discontinuity, *Bull. seism. Soc. Am.*, **61**(1), 79–92.
- Sandwell, D., Sichoix, L., Agnew, D., Bock, Y. & Minster, J.-B., 2000. Near real-time radar interferometry of the  $M_w$  7.1 Hector Mine earthquake, *Geophys. Res. Lett.*, **27**, 3101–3104.
- Sandwell, D.T., 1984. Thermomechanical evolution of oceanic fracture zones, *J. geophys. Res.*, **89**, 11 401–11 413.
- Sauber, J., Thatcher, W., Solomon, S.C. & Lisowski, M., 1994. Geodetic slip rate for the east California shear zone and the recurrence time of Mojave desert earthquakes, *Nature*, **367**, 264–266.
- Savage, J., 1974. Dislocations in seismology, in *Dislocations Theory: A Treatise*, ed. Nabarro, F., Marcel Dekker, New York.
- Savage, J.C., Lisowski, M. & Prescott, W.H., 1980. An apparent shear zone trending north-northwest across the Mojave desert into Owens Valley, Eastern California, *Geophys. Res. Lett.*, **17**(12), 2113–2116.
- Scholz, C.H., 1987. Wear and gouge formation in brittle faulting, *Geology*, **15**, 493–495.
- Segall, P. & Pollard, D., 1980. Mechanics of discontinuous faults, *J. geophys. Res.*, **85**, 4337–4350.
- Shearer, P.M., 1999. *Introduction to Seismology*, Cambridge University Press, New York.
- Sieh, K. *et al.*, 1993. Near-field investigations of the Landers earthquake sequence, *Science*, **260**, 171–176.
- Simons, M., Fialko, Y. & Rivera, L., 2002. Coseismic deformation from the 1999  $M_w$  7.1 Hector Mine, California, earthquake, as inferred from InSAR and GPS observations, *Bull. seism. Soc. Am.*, **92**, 1390–1402.
- Steketee, J.A., 1958a. On Volterra's dislocations in a semi-infinite elastic medium, *Can. J. Phys.*, **36**, 192–205.
- Steketee, J.A., 1958b. Some geophysical applications of the elasticity theory of dislocations, *Can. J. Phys.*, **36**, 1168–1198.
- Thurber, C., Roecker, S., Roberts, K., Gold, M., Powell, L. & Rittger, K., 2003. Earthquake locations and three-dimensional fault zone structure along the creeping section of the San Andreas fault near Parkfield, CA: preparing for SAFOD, *Geophys. Res. Lett.*, **30**, 1112.
- Turcotte, D., Newman, W. & Shcherbakov, R., 2003. Micro and macroscopic models of rock fracture, *Geophys. J. Int.*, **152**, 718–728.
- Vermilye, J. & Scholz, C., 1998. The process zone: a microstructural view of fault growth, *J. geophys. Res.*, **103**, 12 223–12 237.
- Vidale, J. & Li, Y., 2003. Damage to the shallow Landers fault from the nearby Hector Mine earthquake, *Nature*, **421**, 524–526.
- Wang, R., Martin, F. & Roth, F., 2003. Computation of deformation induced by earthquakes in a multi-layered elastic crust—FORTRAN programs EDGRN/EDCMP, *Comp. Geosci.*, **29**, 195–207.
- Weertman, J. & Weertman, J.R., 1964. *Elementary Dislocation Theory*, MacMillan, New York.
- Wilson, B., Dewers, T., Reches, Z. & Brune, J., 2004. Particle size and energetics of gouge from earthquake rupture zones, *Nature*, **434**, 749–752.
- Yu, P., Hu, S.Y., Chen, L.Q. & Du, Q., 2005. An iterative-perturbation scheme for treating inhomogeneous elasticity in phase-field models, *J. Comp. Phys.*, **208**, 34–50.

## APPENDIX: BENCHMARKS

### A.1 Antiplane strain

We compare our numerical solution to analytic and semi-analytic solutions for antiplane, plane-strain and 3-D deformation in a heterogeneous medium. In order to simulate 2-D deformation in our 3-D calculations, we introduce a dislocation extending across the computational grid. The periodicity of the solution, introduced by the Fourier expansion, makes the source effectively infinite in the along-strike direction. In Fig. A1(a), a screw dislocation extends from both ends of the grid, and the resulting deformation is antiplane (the only non-zero component of displacement is along strike). Displacements across a fault exhibit a characteristic arc-tangent profile. In Fig. A1(b), an infinitely long edge dislocation cuts the volume, representing plane strain (the only non-zero component of displacement orthogonal to the fault strike). Benchmarks for 3-D deformation are computed for finite faults.

First we consider cases of a screw dislocation in a vertically stratified elastic half-plane. The modelled domain is composed of a strip of rigidity  $G_1$ , extending from the surface to depth  $H$ , and a bottom half-plane of rigidity  $G_2$ . Fig. A2(a) shows the surface displacement profile corresponding to profile A–A' in Fig. A1 (dashed line) along with the analytic solution for the case of a infinitely long vertical strike-slip fault extending from the surface to a depth of  $0.8 H$  in a homogeneous medium ( $G_1 = G_2$ ). The numerical error, shown on the right-hand panel of Fig. A2(a), increases away from the source, due to the periodicity of the Fourier domain solution. Within an across-fault distance of ten fault lengths, error does not exceed 0.5 per cent compared to the analytic solution (Weertman & Weertman 1964; Rybicki 1971).

We use the perturbation method to compute the deformation in the case of the rigidity contrast  $G_2/G_1 = 1.5$ . Left-hand panel of

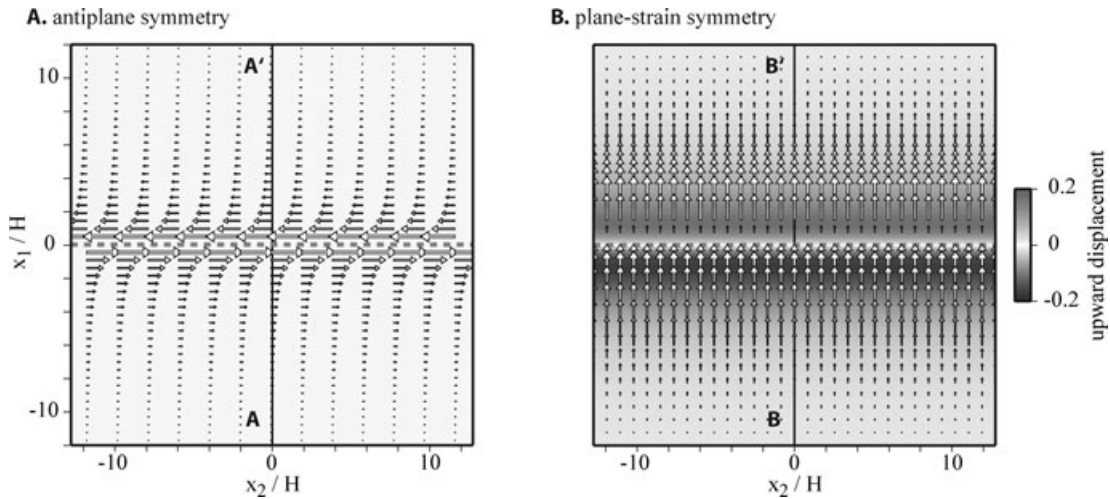
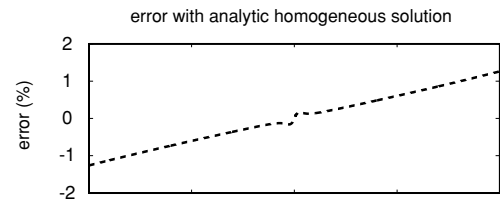
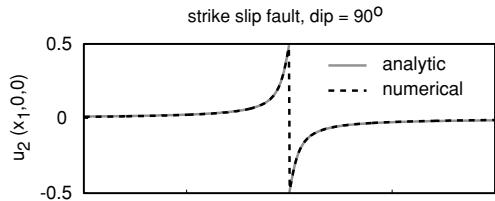
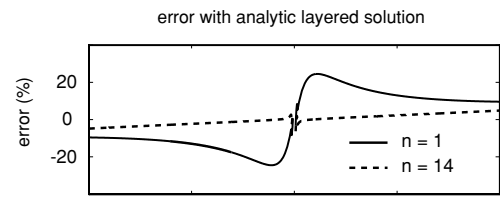
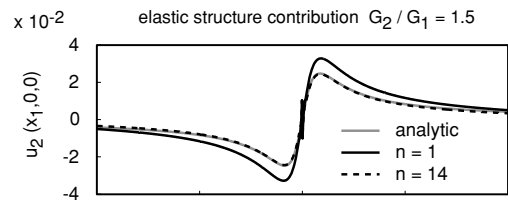


**Figure A1.** 3-D calculation with axes of symmetry. Horizontal ( $u_1$ ,  $u_2$ ), and vertical  $u_3$  surface displacements are represented by white arrows and the background colour, respectively. (a) An infinitely long strike-slip fault (dashed line) creates an antiplane symmetry (no vertical displacement). (b) An infinitely long edge dislocation creates a plane-strain symmetry in the 3-D computational volume.

**A. Homogeneous half space**



**B. Plate over half space, perturbation method**



**C. Plate over half space, successive over-relaxation method**

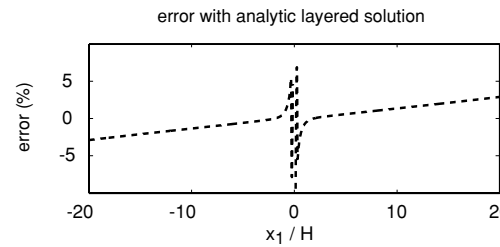
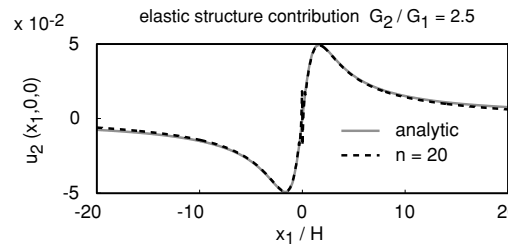


**Figure A2.** Antiplane benchmarks along profile A–A’ in Fig. A1 in the case of a vertical left-lateral strike slip fault. (a) The numerical and analytical solutions for a homogeneous half-space are shown in left-hand panel. The relative error is shown in the right-hand panel and remains smaller than 0.5 per cent 10 fault lengths away from the fault trace. (b) Perturbation method. The difference between the surface displacements corresponding to a heterogeneous elastic structure and a homogeneous half-space. The elastic structure consists in a plate of rigidity  $G_1 = 1$ , extending from the surface to the depth  $H$ , and the bottom half-space of rigidity  $G_2 = 1.5$ . The strike slip fault extends from the surface to the locking depth  $0.8 H$ . Numerical solution is shown at 1 and 14 iterations of the perturbation method. (c) Successive over relaxation method (SOR). Results similar to (b) but with a higher elastic contrast  $G_2/G_1 = 2.5$ . Convergence is obtained after 20 iterations.

Fig. A2(b) shows the heterogeneous contribution (the difference between surface displacements in heterogeneous and homogeneous media). The first iteration of the perturbation method is shown in solid line and over-estimates the effect of the rigidity contrast. Corresponding error is about 20 per cent compared to the analytic result. After 14 iterations, convergence criterion (eq. 39 in the main text) is satisfied and error is comparable to the case of a homogeneous elastic structure.

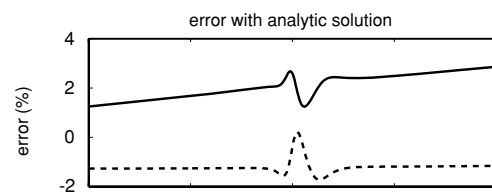
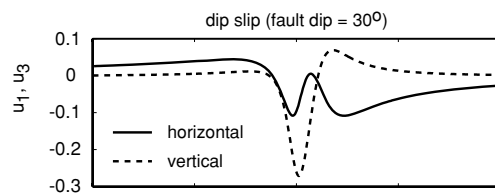
We use the SOR method to compute the displacements in the case of the elastic contrast  $G_2/G_1 = 2.5$ . Convergence criterion is reached after 20 iterations. Numerical and analytic solutions for the heterogeneous structure and corresponding errors are shown in Fig. A2(c). Error does not exceed 5 per cent except in a small vicinity around the dislocation where it reaches a maximum of 10 per cent. In case of a large elastic contrast, the homogenized elastic parameters must minimize the effective elastic contrast and does not correspond to a value of rigidity around the fault. The difference in effective

stress is compensated at each iteration after estimating the amplitude of stress near the fault. Numerical evaluation of stress in the fault zone is complicated by the presence of the discontinuity and results in a greater final error at the fault location (see right-hand panel in Fig. A2c). Overall, our 2-D numerical solutions performed in a 3-D computational grid compare well to the analytic solutions for antiplane deformation. The use of the SOR method allows us to consider such crustal structures with large variations in rigidity.

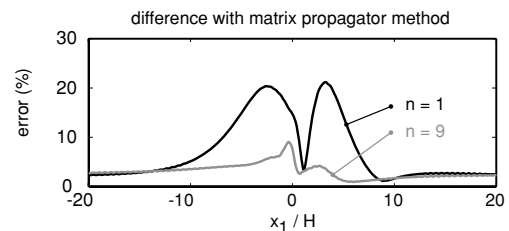
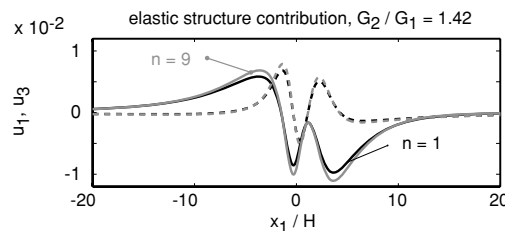
## A.2 Plane strain

Next, we consider the case of plane-strain deformation. Fig. A3 shows the displacement field along profile B–B' in Fig. A1. The elastic structure consists of a strip of thickness  $H$  with Lamé parameters  $\lambda_1 = G_1$  overlying a half-plane with elastic parameters  $\lambda_2 = G_2$ . An edge dislocation with unit slip, dipping  $30^\circ$ , starts in the bottom layer at depth  $1.5H$  and extends to depth  $3.5H$ .

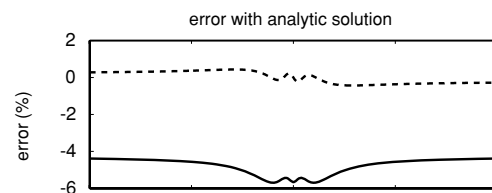
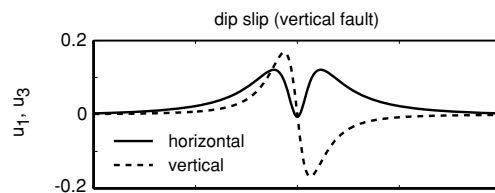
### A. Homogeneous half space



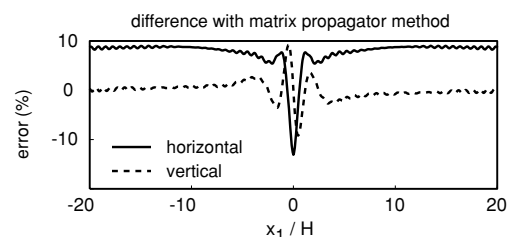
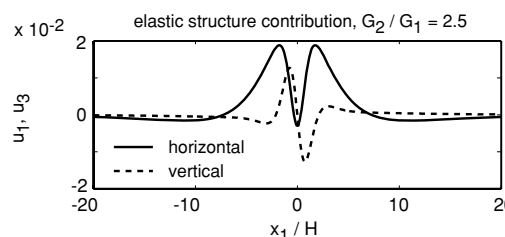
### B. Plate over half space, perturbation method



### C. Homogeneous half space



### D. Plate over half space, SOR method



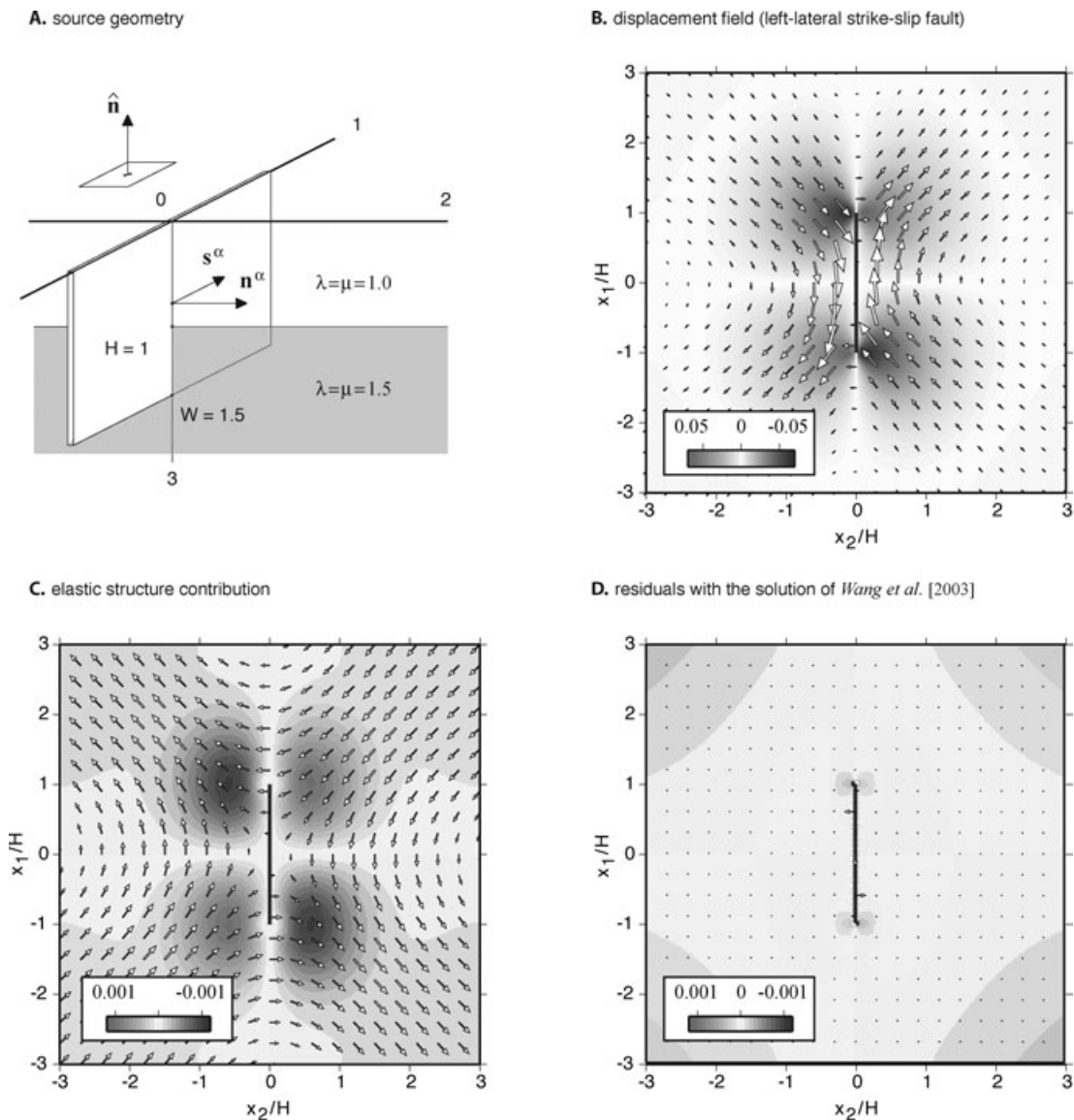
**Figure A3.** Plane-strain benchmarks along profile B–B' in Fig. A1. (a) Surface displacements corresponding to a unit slip occurring on a buried edge dislocation dipping  $30^\circ$ . Numerical error (right-hand panel) does not exceed 3 per cent compared to analytic solution. (b) Perturbation method. An more compliant plate, with  $\lambda_1 = G_1 = 0.7$  and extending from the surface to a depth  $H$ , overrides a half-space of Lamé parameters  $\lambda_2 = G_2 = 1$ . Left-hand panel shows first iteration ( $n = 1$ ) and converged ( $n = 9$ ) solutions of the perturbation method. Norm of error corresponding to the converged solution remains smaller than 5 per cent compared to results of the matrix propagator method. (c) Same as (a) but with a vertical dip slip fault. (d) Successive over relaxation (SOR) method. Solution displacements and relative error compared to the matrix propagator method for the layered structure of (b) with a greater elastic contrast  $G_2/G_1 = 2.5$  and a constant  $\lambda_1 = \lambda_2 = 1$ .

Fig. A3(a) shows the surface displacement in the case of a homogeneous medium. Corresponding error compared to analytic solution (Savage 1974; Niazy 1975) is shown on right-hand panel and does not exceed 3 per cent. The constant shift error is an artifact due to periodicity of the Fourier domain solutions.

We use the perturbation method to evaluate the surface displacement in the case of a more compliant top strip with  $G_1/G_2 = 0.7$  (Poisson's ratio is the same for the two layers). We choose the homogenized elastic parameters corresponding to the bottom layer, where the fault is located. We compare our numerical solution with the displacement obtained using the matrix propagator method of P. Segall (personal communication, 2008). Fig. A1(b) shows the elastic structure contribution, the difference between heterogeneous and homogeneous solutions. First approximate solution, at first iteration of the perturbation method, is an under-estimate the final solution. Convergence criterion is reached after 9 iterations with a final error smaller than about 5 per cent of the expected elastic contribution signal. Note that the elastic contribution is one order of magnitude

smaller than the total displacement. The difference between the total displacements obtained using the propagator-matrix method or our approach is therefore barely distinguishable. The surface displacement due to a vertical edge dislocation extending from depth  $1.5H$  to  $3.5H$  is shown in Fig. A1(c). Horizontal displacement error is characterized by a constant bias of about 5 per cent of the expected signal. Vertical displacement is antisymmetric and does not display such constant bias. Error in the vertical direction is limited to about 0.5 per cent.

We use the SOR method to compute the displacement in the presence of a large elastic contrast between the horizontal layers. We use  $\lambda_1 = G_1 = 1$  in the top layer and  $\lambda_2 = 1$  and  $G_2 = 2.5$  in the bottom layer. Convergence is reached after 18 iterations. We compare our solutions with results from the matrix propagator technique. Horizontal displacements exhibit a bias close to 10 per cent of the expected signal. Error in the vertical direction is limited to about 2 per cent except close to the fault for reasons discussed above in the case of antiplane strain. We conclude that our



**Figure A4.** 3-D benchmark. (a) A strike-slip fault fractures crustal areas with different elastic moduli. The rigidity in the bottom half-space is 50 per cent higher than in the top plate. (b) The displacement field at the surface of the half-space. (c) Difference between the displacement field in (b) and the corresponding homogeneous solution where  $G_1 = G_2$ . (d) Residuals between our Fourier domain semi-analytic result and the result of Wang *et al.* (2003).

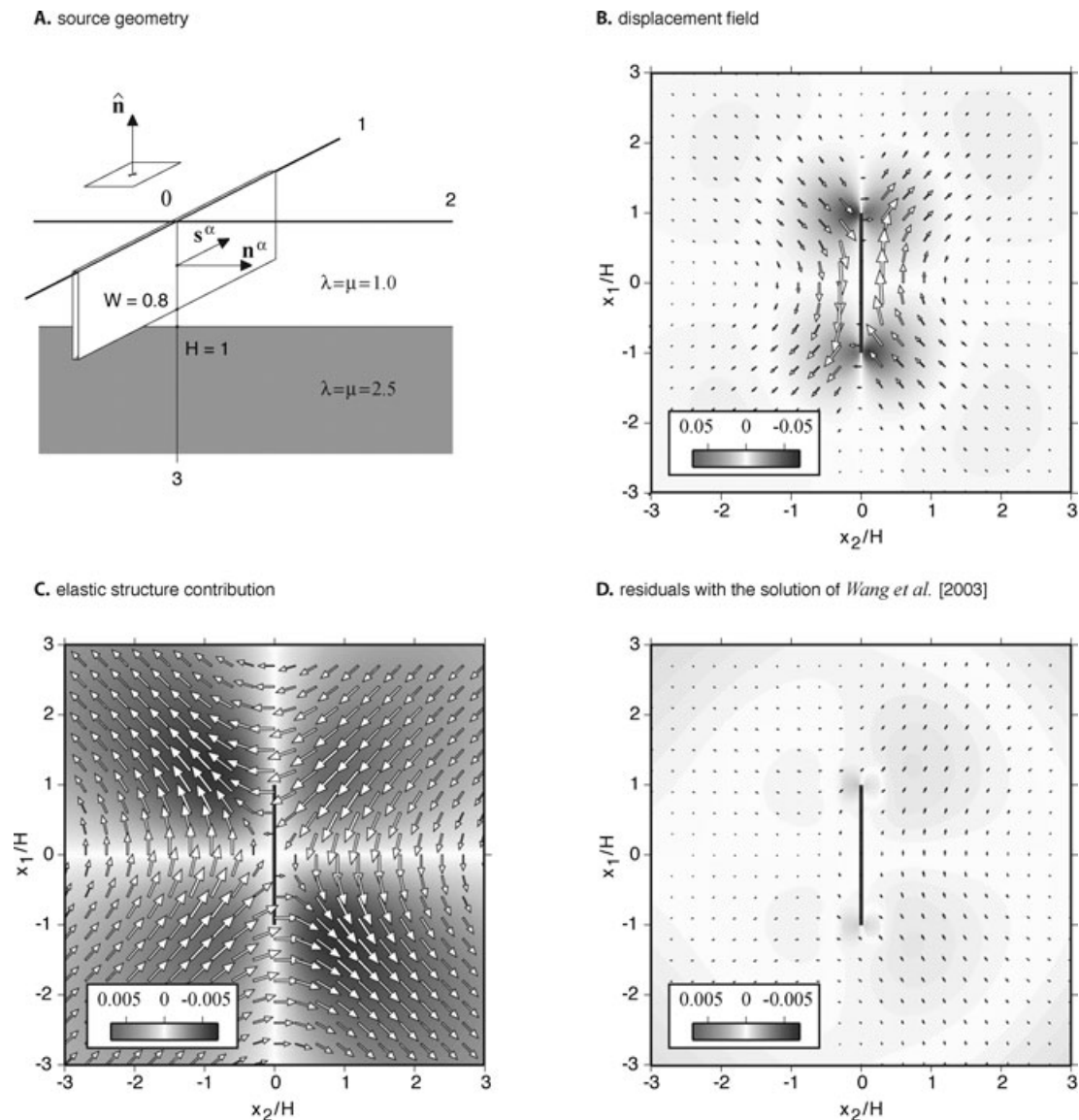


**Figure A5.** 3-D benchmark. (a) A strike-slip fault breaks the upper crust. The rigidity in the bottom half-space is 2.5 times higher than in the top plate. (b) The displacement field at the surface of the half-space. (c) Elastic structure contribution. (d) Residuals between our Fourier domain semi-analytic result and the result of Wang *et al.* (2003).

2-D simulations for plane strain and antiplane problems compare well with available analytic or semi-analytic solutions.

### A.3 3-D deformation

We compare our 3-D numerical models to the Green function approach of Wang *et al.* (2003) for 3-D deformation in a vertically stratified elastic half-space. We introduce a finite strike-slip fault in a semi-infinite solid where the elastic moduli increase at the transition depth  $H$ . Poisson's ratio ( $\nu = 0.25$ ) is identical in each layer but the shear modulus is increased by 50 per cent in the bottom half-space compared to its value in the overlying plate. The left-lateral strike-slip fault extends vertically from the surface to a depth of  $1.5H$  and is  $L = 2W$  long in the along-strike direction. This geometric configuration allows us to evaluate our modelling of dislocations intersecting materials with dissimilar elastic moduli. Fig. A4(a) shows the horizontal (black arrows) and vertical (background colour) dis-

placements that represent the difference between the displacement field obtained with a heterogeneous medium and with a homogeneous medium, respectively. The fault trace is indicated by the black line in the  $x_1$ -direction (north). The final solution is obtained with the perturbation method after 14 iterations. Fig. A4(b) shows the comparison with the solution of Wang *et al.* (2003), using the same scaling for arrows and same colour scale as in Fig. A4(a). Some large residuals in the horizontal direction appear only on the fault trace and are due to the fact that slip is not single-valued at the fault interface. Residuals in the vertical direction occur near the quadrants of the computational grid due to the effect of periodicity of the Fourier domain solution. Despite some small differences inherent to the method, our Fourier domain perturbation approach compares very well with the Green function method of Wang *et al.* (2003). In a test with a large increase of elastic moduli with depth, we introduce a finite strike-slip fault extending from the surface to a depth of  $0.8H$  (see Fig. A5). We use the SOR method to evaluate the deformation in the computational volume. Our numerical

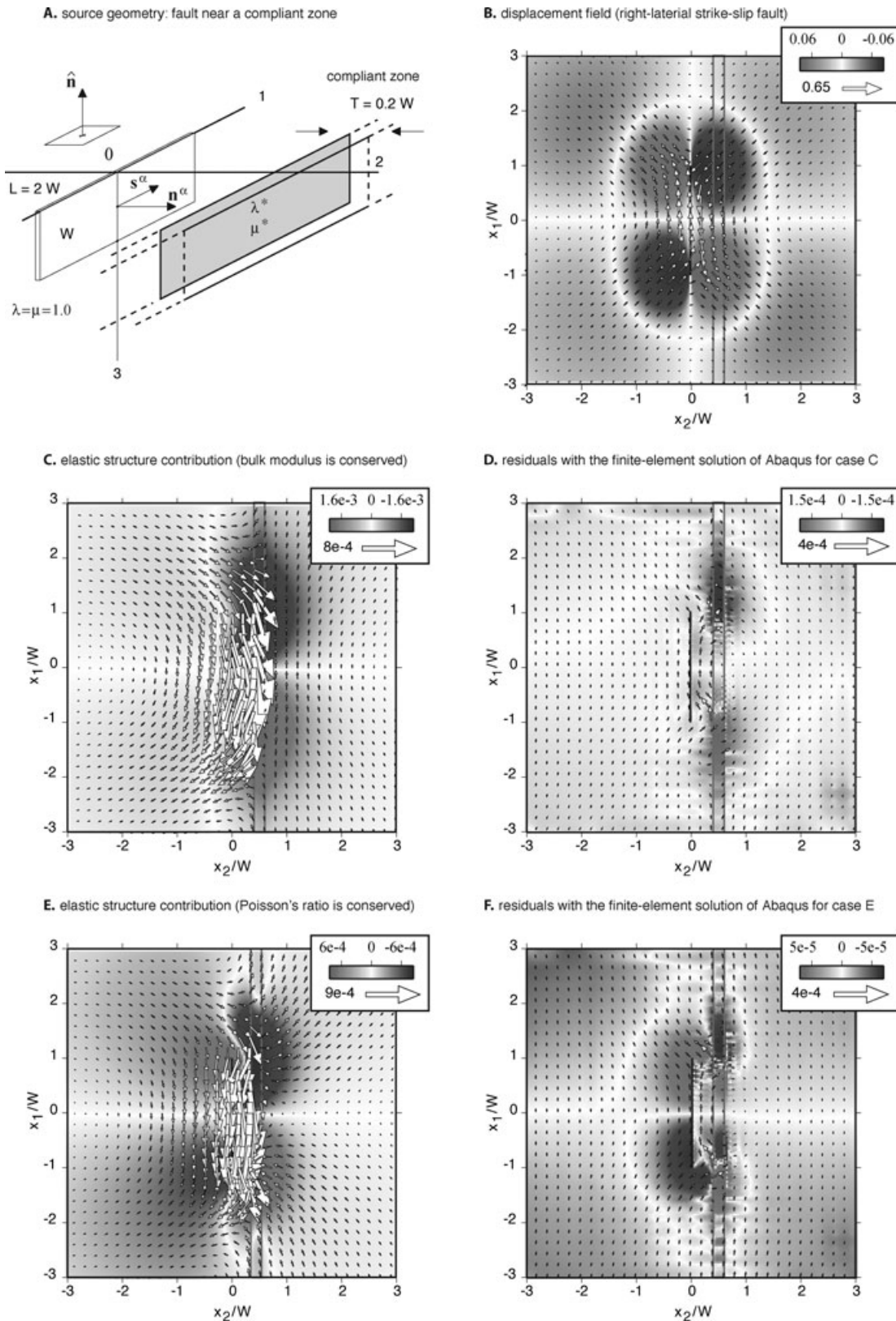


**Figure A6.** Lateral variations of elastic moduli. (a) A right-lateral strike-slip fault slips near a compliant zone. The compliant zone is infinitely long and 10 km deep with a 10 per cent reduction in shear modulus compared to ambient crust. (b) The displacement field at the surface of the half-space. (c) Elastic structure contribution for the case when the bulk modulus is uniform in the half-space. (d) Residuals between our Fourier-domain semi-analytic result and the result of finite-element calculation with Abaqus for case (c). (e) Elastic structure contribution for the case when Poisson's ratio is uniform in the half-space. (f) Residuals between Fourier-domain solution and results from finite-element calculations corresponding to case (e).

estimate of 3-D elastostatic deformation in a heterogeneous half-space with large variations in elastic moduli also favourably compares to results obtained with the Green function approach of Wang *et al.* (2003).

Finally, we test the proposed method for a case of lateral variations in elastic moduli. We compare the predictions of our model with finite-element calculations using the Abaqus software. We introduce a right-lateral strike-slip fault of length  $L$  striking north–south along the  $x_1$ -axis from the surface to a depth  $W$ . An infinitely long compliant zone runs parallel to the fault. The fault and the centre of the compliant zone are separated by a distance  $W/2$ . The geometry and resulting calculations are shown in Fig. A6. We create a mesh with increasing node density closer to the fault and the compliant zone. The minimum distance separating the nodes is  $W/30$ . For the Fourier-domain solution, we use a uniform sampling of  $W/30$  and a computation grid of  $256 \times 256 \times 256$  nodes. We consider two cases. In a first simulation, the shear modulus in the compliant zone is reduced by a factor of 10 per cent and the Poisson's ratio  $\nu = 1/4$  is uniform in the half-space. In a second simulation, the shear modulus is reduced by 10 per cent compared to surrounding solid, but the bulk modulus is uniform in the half-space. In this second case, Poisson's ratio is  $\nu = 0.26$  in the compliant zone. Using the perturbation approach, we obtain convergence in both cases after

four iterations. The perturbation due to the presence of the compliant zone in both cases represents about 5 per cent of the maximum signal in a uniform half-space. The corresponding surface displacement is shown in Fig. A6(a). The elastic contribution is shown in Figs A6(c) and (e) for the uniform bulk modulus and uniform Poisson's ratio, respectively. The pattern of horizontal displacements, shown by the arrows in Fig. A6, is comparable in both cases, with additional displacements to the east of the fault. We observe more vertical displacement to the west of the fault in the case where Poisson's ratio is conserved. The difference between predictions of our approach and the finite-element solution is shown in Figs A6(d) and (f), for the uniform bulk modulus and the uniform Poisson's ratio, respectively. In the course of our numerical validation, we have noted that the benchmark corresponding to the conserved bulk modulus (Figs A6c and d) could be only be matched with the inclusion of equivalent surface traction, as indicated by eq. (21). The residuals represent about 10 per cent of the corresponding elastic contribution signal and about 1 per cent of the cumulative displacement. There is an overall excellent fit between our Fourier domain solutions and the finite-element calculations. We conclude that our semi-analytic iterative approach can be successfully used to model crustal deformation due to faulting in the Earth with realistic spatial distribution of elastic moduli.